

Modelling and Inversion of Cross-Well Electrical Resistivity Tomography Data

Submitted in partial fulfilment of the requirements for the degree of
Master of Science

By

Nimatullah

Roll No. – 22N0005

M.Sc. Applied Geophysics

Under the supervision of
Prof. Anand Singh



Department of Earth Sciences

Indian Institute of Technology Bombay

2024

Approval Sheet

The M.Sc. dissertation report entitled “**Modeling and inversion of cross well Electrical Resistivity Tomography data**” prepared by Nimatullah (Roll No. – 22N0005) is hereby approved for submission.

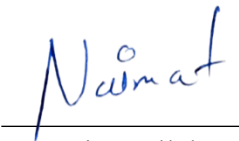
Prof. Anand Singh
(Supervisor)

Prof. Mohan Gollapally
(Examiner)

Prof. Anand Singh
(Examiner)

Declaration

I hereby affirm that this written submission is a true representation of my own thoughts and ideas, expressed in my own words. In instances where I have incorporated the ideas or words of others, I have diligently cited and referenced the original sources. Furthermore, I attest that I have upheld all principles of academic honesty and integrity throughout the creation of this submission. I have not engaged in any misrepresentation, fabrication, or falsification of ideas, data, facts, or sources. I acknowledge that any breach of these principles may result in disciplinary measures from the Institute and potential legal consequences from sources that have not been appropriately cited or from which proper permissions have not been obtained as required.


Nimatullah

Applied Geophysics

Roll no.-22N0005

Acknowledgments

I want to express my gratitude for the chance to work on this project and give a big thanks to Professor Anand Singh for believing in me and guiding me every step of the way. His advice has been invaluable, and I couldn't have done it without him.

I also want to thank the lab and support staff for providing us with everything we needed to get the job done. Their help made a huge difference.

And of course, a big shoutout to my friends and family for always being there for me, cheering me on, and helping me through any challenges that came up. I couldn't have finished this project without their support.

TABLE OF CONTENTS

APPROVAL SHEET	2
DECLARATION	3
ACKNOWLEDGMENTS	4
TABLE OF CONTENTS	5
LIST OF FIGURES	7
ABSTRACT	10
CHAPTER-1	11
INTRODUCTION	11
1.1 DC RESISTIVITY METHODS.....	11
1.2 DATA ACQUISITION	12
1.2.1 Vertical electrical sounding	12
1.2.1.1 Application of VES.....	13
1.2.2 Imaging	13
1.2.2.1 Application of Imaging.....	14
1.2.3 Continuous profiling	14
1.2.3.1 Application of Continuous profiling.....	15
1.2.4 CROSS-WELL ERT	15
1.2.4.1 Application of cross well ERT	17
CHAPTER-2.....	18
PROCESSING AND FORWARD MODELLING	18
2.1 PROCESSING OF CROSS-WELL ELECTRICAL RESISTIVITY TOMOGRAPHY DATA.....	18
2.2 NOISE IN CROSS-WELL ELECTRICAL DATA	18
2.3 NOISE REMOVAL.....	18
2.3 FORWARD MODELLING.....	19
2.3.1 Finite element methods (FEM).....	19
2.3.2 Calculation of the total potential.....	19
2.3.3 Mesh generation and refinement	20
2.4 MODELS.....	21
2.4.1 Model 1	21
2.4.2 Model 2	22
CHAPTER-3.....	24

INVERSION AND MODEL RESOLUTION	24
3.1 INVERSION	24
3.2 INVERSION OF CROSS-WELL ERT DATA	24
3.2.1 Choice of Norm	26
3.2.2 Minimization of Inverse Problem	26
3.4 CROSS WELL ERT INVERSION WORKFLOW	29
3.5 MODEL RESOLUTION MATRIX	29
3.6 MODEL RESOLUTION ANALYSIS	30
CHAPTER 4	31
RESULT	31
4.1 INVERSION RESULTS	31
4.1.1 Model 1	31
Homogeneous Subsurface Medium	32
4.1.2 Model 2	33
Heterogeneous Subsurface Structures	34
4.1.3 Analysis of Inversion Results	34
4.2 MODEL RESOLUTION ANALYSIS: EVALUATING RESOLUTION QUALITY	35
4.2.1 Synthetic Model 1	36
4.2.2 Synthetic Model 2	37
4.2.3 Synthetic Model 3	38
4.2.4 Synthetic Model 4	39
4.2.5 Synthetic Model 5	40
4.2.6 Synthetic Model 6	41
4.2.7 Synthetic Model 7	42
4.2.8 Synthetic Model 8	43
4.2.9 Analysis of Model Resolution	44
4.2.9 Implications for Subsurface Imaging	44
CHAPTER 5	45
CONCLUSIONS	45
REFERENCES	46

List of Figures

Chapter-1

Figure 1. 1 The basic concept of DC resistivity measurements (Source: subsurface insights)	11
Figure 1. 2 VES representative curves of the Q-type (a), H-type (b).....	12
Figure 1. 3 Wenner array (“a” is electrode spacing) and distribution of electric field underneath (after Wiwattanachang, and Giao, 2011).....	13
Figure 1. 4 Electrode locations and their corresponding collected data using the Wenner configuration (after Wilson, 2022)	14
Figure 1. 5 . Contour plot of the collected apparent resistivity data (after Wilson, 2022)	14
Figure 1. 6 Schematic diagram of the deep-towed marine electrical resistivity tomography system. Two current electrodes C1 and C2 and eight potential electrodes P1–P8 are attached to the cable together with two reference electrodes COM1 and COM2 (after Ishizu, 201).....	15
Figure 1. 7 Schematic diagram of the deep-towed marine electrical resistivity tomography system. Two current electrodes C1 and C2 and eight potential electrodes P1–P8 are attached to the cable together with two reference electrodes COM1 and COM2 (after Ishizu, 201).....	15
Figure 1. 8 Pseudo-section of the response from the inverted model (after Ishizu, 2019).....	15
Figure 1. 9 Cross Well ERT Acquisition.....	17

Chapter-2

Figure 2. 1 a.) Discretisation in unstructured triangles b.) Mesh Refinement.....	21
Figure 2. 2 Simulation of CO ₂ injection and spread within a homogeneous subsurface medium. The polygon represents the injected CO ₂ body, with changing resistivity values over time (t1-t4). The coordinates of the body's vertices and the resistivity of the medium and body are detailed at each time step. This dynamic model provides insights into the behavior and impact of CO ₂ injection in a controlled environment	22
Figure 2. 3 Simulation of CO ₂ injection and spread within a heterogeneous subsurface. The polygon represents injected CO ₂ , with changing resistivity over time (t1-t4). Varying colors indicate the heterogeneous nature of the subsurface. Insights gained from this model aid in understanding CO ₂ behaviour in realistic geological settings	23

Chapter-3

Figure 3. 1 Convergence curve of the data error as a function of the iteration number	25
Figure 3. 2 Minimisation of RMS error in successive iterations and parameter Triangular mesh Grid to carry out inversion for individual cells	25
Figure 3. 3 Flow chart of the inversion procedure.....	29

Chapter-4

Figure 4. 1 Simulation of CO ₂ injection and spread within a homogeneous subsurface medium. The polygon represents the injected CO ₂ body, with changing resistivity values over time (t ₁ -t ₄). The coordinates of the body's vertices and the resistivity of the medium and body are detailed at each time step. This dynamic model provides insights into the behavior and impact of CO ₂ injection in a controlled environment	31
Figure 4. 2 Inverse modeling results show the inferred CO ₂ distribution over time (t ₁ -t ₄), along with the evolving resistivity values of the injected CO ₂ body. This visualization provides valuable insights into the spatial distribution and dynamic behavior of injected CO ₂ within the subsurface medium	32
Figure 4. 3 Simulation of CO ₂ injection and spread within a heterogeneous subsurface. The polygon represents injected CO ₂ , with changing resistivity over time (t ₁ -t ₄). Varying colors indicate the heterogeneous nature of the subsurface. Insights gained from this model aid in understanding CO ₂ behaviour in realistic geological settings	33
Figure 4. 4 Inverse modeling of CO ₂ injection and propagation within a heterogeneous subsurface medium. The inverted results depict the inferred spatial distribution of CO ₂ over time (t ₁ -t ₄), considering the dynamic changes in resistivity associated with the injected CO ₂ body. The diverse colors reflect the heterogeneity of the subsurface, providing valuable insights into CO ₂ behavior within realistic geological formations.	34
Figure 4. 5 Cross-Well Synthetic Data Analysis: Considering a single layer model with the resistivity values of $\rho_1 = 100 \Omega \cdot m$ for the background medium and $\rho_2 = 10 \Omega \cdot m$ for the anomalous body:(a) Synthetic two-layer model at time t ₁ , with the vertices defining the body located at coordinates 15, 16, 17, 26, 27, and 28 while maintaining the resistivity of the medium at 100 $\Omega \cdot m$ and the resistivity of the body at 10 $\Omega \cdot m$.(b) Inverted electrical resistivity imaging model based on the synthetic data.(c) Model Resolution Matrix depicting the resolution quality of the inverted model.	36
Figure 4. 6 Cross-Well Synthetic Data Analysis: (a) Synthetic two-layer model at time t ₂ , with the vertices defining the body shifted to coordinates 12, 13, 14, 30, 31, and 32 while maintaining the resistivity of the medium at 100 $\Omega \cdot m$ and adjusting the resistivity of the body to 15.85 $\Omega \cdot m$.(b) Inverted electrical resistivity imaging model based on the synthetic data.(c) Model Resolution Matrix depicting the resolution quality of the inverted model.....	37
Figure 4. 7 Cross-Well Synthetic Data Analysis: (a) Synthetic two-layer model at time t ₂ , with the vertices defining the body shifted to coordinates 10, 11, 12, 34, 35, and 36 while maintaining the resistivity of the medium at 100 $\Omega \cdot m$ and adjusting the resistivity of the body to 25.12 $\Omega \cdot m$.(b) Inverted electrical resistivity imaging model based on the synthetic data.(c) Model Resolution Matrix depicting the resolution quality of the inverted model.....	38

Figure 4. 8 Cross-Well Synthetic Data Analysis: (a) Synthetic two-layer model at time t_2 , with the vertices defining the body shifted to coordinates 10, 11, 12, 35, 36, and 37 while maintaining the resistivity of the medium at $100 \Omega \cdot m$ and adjusting the resistivity of the body to $39.81 \Omega \cdot m$.(b) Inverted electrical resistivity imaging model [$\Omega \cdot m$] based on the synthetic data.(c) Model Resolution Matrix depicting the resolution quality of the inverted model.	39
Figure 4. 9 (a)Synthetic model representing a heterogeneous medium characterized by diverse resistivity values. Initially, at time t_1 , the resistivity values of the layers were as follows: approximately 125.89 ohm-m for both the first and second layers, while the third and fourth layers exhibited resistivities of 100 ohm-m each. .(b) Inverted electrical resistivity imaging model [$\Omega \cdot m$] based on the synthetic data.(c) Model Resolution Matrix depicting the resolution quality of the inverted model.....	40
Figure 4. 10 (a) Synthetic model representing a heterogeneous medium characterized by diverse resistivity values. Initially, at time t_1 , the resistivity values of the layers were as follows: approximately 158.49 ohm-m for both the first and second layers, while the third and fourth layers exhibited resistivities of 100 ohm-m each. .(b) Inverted electrical resistivity imaging model [$\Omega \cdot m$] based on the synthetic data.(c) Model Resolution Matrix depicting the resolution quality of the inverted model.....	41
Figure 4. 11 (a) Synthetic model representing a heterogeneous medium characterized by diverse resistivity values. Initially, at time t_1 , the resistivity values of the layers were as follows: approximately 199.53199.53 ohm-m for both the first and second layers, while the third and fourth layers exhibited resistivities of 100 ohm-m each. .(b) Inverted electrical resistivity imaging model [$\Omega \cdot m$] based on the synthetic data.(c) Model Resolution Matrix depicting the resolution quality of the inverted model.....	42
Figure 4. 12 (a) Synthetic model representing a heterogeneous medium characterized by diverse resistivity values. Initially, at time t_1 , the resistivity values of the layers were as follows: approximately 223.87223.87 ohm-m for both the first and second layers, while the third and fourth layers exhibited resistivities of 100 ohm-m each. .(b) Inverted electrical resistivity imaging model [$\Omega \cdot m$] based on the synthetic data.(c) Model Resolution Matrix depicting the resolution quality of the inverted model.....	43

Abstract

This study delves into the advancements and applications of electrical resistivity methods, particularly focusing on cross-well Electrical Resistivity Tomography (ERT) for subsurface imaging. Traditional direct current (DC) resistivity methods provide valuable insights into subsurface resistivity distributions, but with limitations in depth penetration and resolution. To overcome these limitations, the study presents a novel approach utilizing cross-well ERT, which involves strategically placed electrodes within boreholes for enhanced depth penetration and resolution. The abstract outlines the methodology and data acquisition techniques, including vertical electrical sounding, imaging, continuous profiling, and cross-well ERT, along with their respective applications. Noise analysis and removal techniques are discussed, followed by forward modeling methodologies using finite element methods and mesh generation strategies. Two synthetic models are presented to simulate CO₂ injection and spread within homogeneous and heterogeneous subsurface mediums, demonstrating the dynamic behavior and impact of CO₂ within controlled environments. The inversion process for cross-well ERT data is detailed, including the choice of norm, minimization of inverse problems, and inversion results for the presented models. In summary, this study contributes to the advancement of subsurface imaging techniques, particularly in the context of CO₂ monitoring and geological investigations. The utilization of cross-well ERT offers promising avenues for detailed subsurface imaging, with implications for various fields such as environmental monitoring, geological exploration, and hazard assessment.

Chapter-1

Introduction

1.1 DC Resistivity Methods

The direct current (DC) resistivity method measures subsurface resistivity. In this method, we inject electric currents into the ground and measure electric voltages at different locations; the method gives information about the distribution of electrical resistivity in the subsurface. The apparent resistivity (ρ_a) is calculated by measuring the potential difference (ΔV) between different pairs of electrodes, considering the current (I) and a geometric factor (G) specific to the electrode array used.

$$\rho_a = \frac{G\Delta V}{I}$$

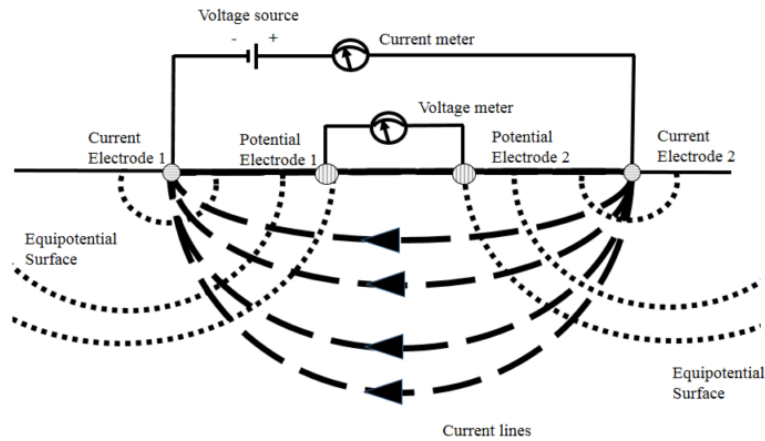


Figure 1. 1 The basic concept of DC resistivity measurements (Subsurface Insights, n.d.)

However, the measured data alone do not directly offer the desired information. To extract meaningful insights, inversion techniques are essential. The inverse DC resistivity problem is inherently challenging due to the problem is ill-posed concerning data errors and incomplete data sets. Initially, resistivity soundings were employed to assess horizontal layers of varying conductivity. Modern advancements involve profile measurements using pre-installed multielectrode lines, offering good observation for investigating 2-D structures. For 3-D exploration, large electrode arrays or numerous parallel profile lines are employed to facilitate comprehensive investigations.

Despite these advancements, the depth of penetration and resolution of DC 3D resistivity methods have limitations. In this study, we present a novel approach focusing on Modelling and Inversion of Cross-Well Electrical Resistivity Tomography (ERT) data. This method

involves drilling boreholes and placing electrodes within them, following the same principles as the DC resistivity method.

By adopting a cross-well ERT approach, we aim to overcome the limitations of traditional DC 3D resistivity methods. The utilization of boreholes and strategically placed electrodes enhances depth penetration and resolution, making it a promising avenue for detailed subsurface imaging. Our study contributes to advancing the understanding of subsurface structures through innovative modeling and inversion techniques, paving the way for improved accuracy and reliability in geological investigations.

1.2 Data Acquisition

1.2.1 Vertical electrical sounding

A vertical electrical sounding array is technique for data acquisition, involving the placement of two current electrodes (AB) and two potential electrodes (MN). These electrodes are initially positioned at the midpoint and varied distances. The survey progresses by moving the current electrodes outward, while the potential electrodes are kept stationary until the measured voltage reaches a threshold too small to be accurately recorded. This systematic approach allows for the collection of meaningful data across different depths, contributing to a comprehensive vertical profile of subsurface electrical resistivity.

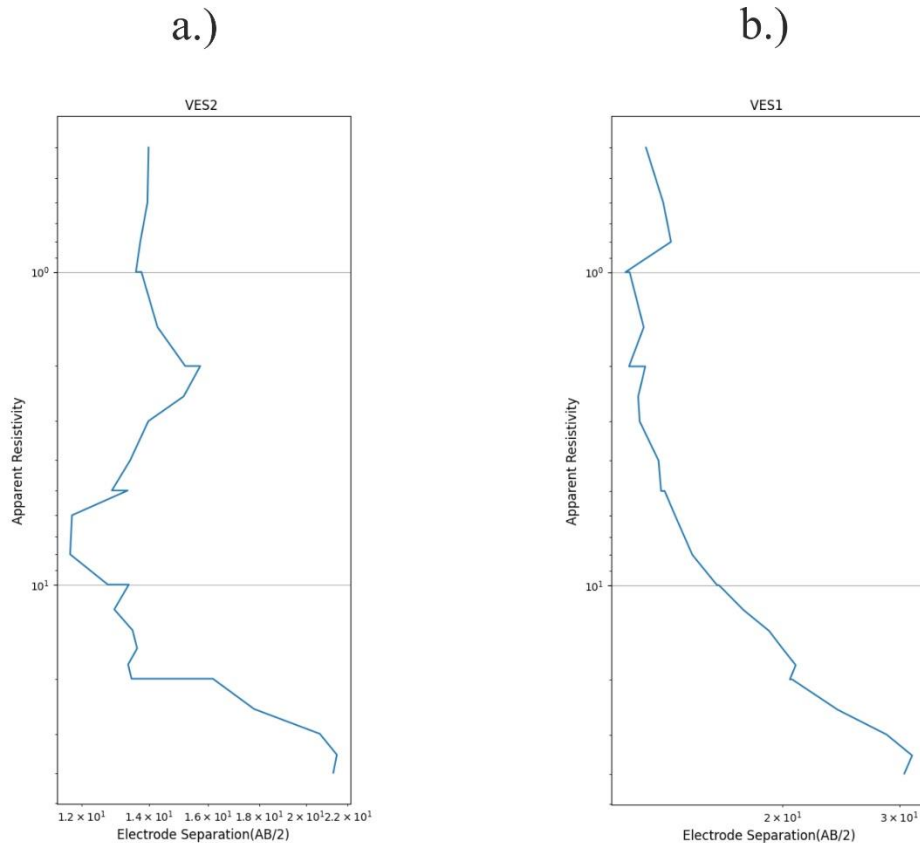


Figure 1. 2 VES representative curves of the Q-type (a), H-type (b)

1.2.1.1 Application of VES

- Identifying unsaturated and saturated layers: VES can identify unsaturated and saturated layers below the surface and aquifer potential.
- Mapping pipeline routes: VES can be used to map pipeline routes.

1.2.2 Imaging

The Wenner electrode array is a soil resistivity measurement technique, having four electrodes A, M, N, and B. These electrodes are arranged in a straight line at equal intervals. The outer electrodes, A and B, work as current electrodes, while the inner electrodes, M and N, function as potential electrodes. This method gives lateral variations in subsurface resistivity. Widely applied in mineral prospecting, it proves particularly valuable for identifying shear zones, faults, and localized areas exhibiting anomalous conductivity. The simplicity and effectiveness of the Wenner electrode array make it a preferred choice for investigations into the electrical properties of the subsurface.

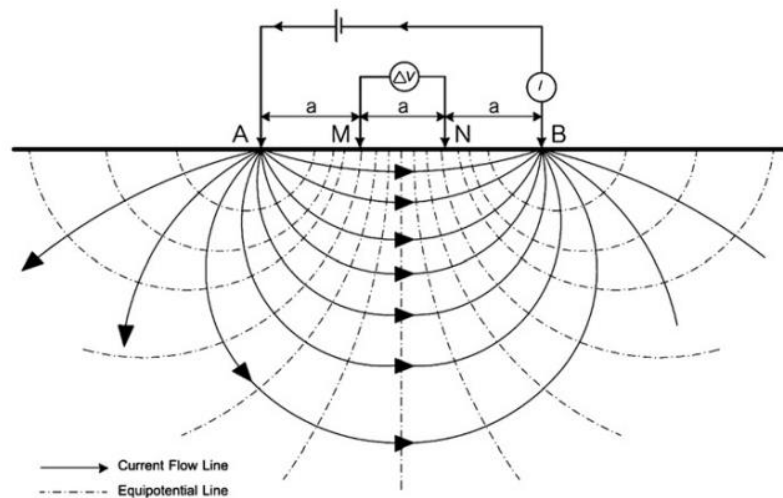


Figure 1. 3 Wenner array (“a” is electrode spacing) and distribution of electric field underneath (N. Wiwattanachang, 2011)

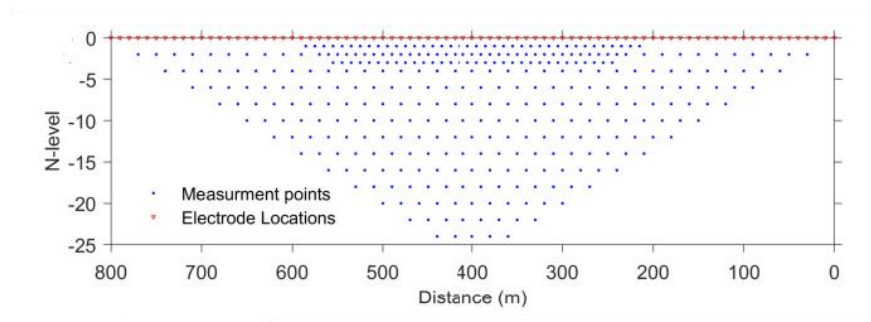


Figure 1. 4 Electrode locations and their corresponding collected data using the Wenner configuration (Wilson, 2022)

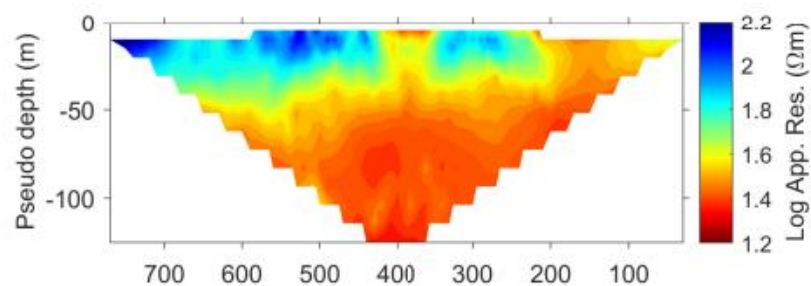


Figure 1. 5 . Contour plot of the collected apparent resistivity data (Wilson, 2022)

1.2.2.1 Application of Imaging

- Imaging is often applied for mapping the resistivity of subsurface materials, helping to distinguish between different soil types and identify bedrock layers.
- In environmental investigations, Imaging can be used to assess the subsurface structure for contamination and monitor groundwater movement.

1.2.3 Continuous profiling

Electrical Resistivity Tomography (ERT) has found applications in terrestrial environments, shallow water regions, and even deep-sea areas. In conducting an ERT survey, an electrical current is introduced between two electrodes, and the resulting voltages are measured across other paired electrodes. The trailing section in this system, known as the long tail, comprises cables with lengths

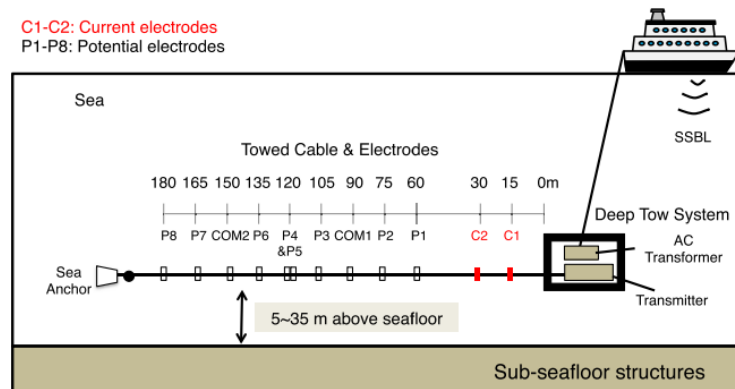


Figure 1. 6 Schematic diagram of the deep-towed marine electrical resistivity tomography system. Two current electrodes C1 and C2 and eight potential electrodes P1–P8 are attached to the cable together with two reference electrodes COM1 and COM2 (Ishizu, 2019)

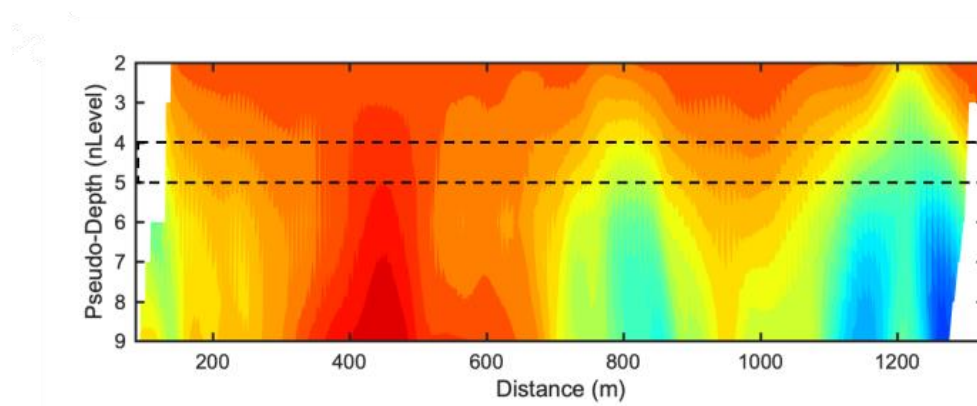


Figure 1. 8 Pseudo-section of the response from the inverted model (Ishizu, 2019)

1.2.3.1 Application of Continuous profiling

- Identification of submarine groundwater discharge (SGD)
- Mapping of fresh/saline-water intrusion

1.2.4 Cross-well ERT

Several electrodes are placed in each hole in electrical contact with the formation (see Figure). Two adjacent electrodes are driven by a known current, and the resulting voltage difference is measured between all other adjacent pairs of electrodes (in both boreholes). Then, the known current is applied to two other adjacent electrodes and the voltage is again measured between all other adjacent pairs. This process is repeated until current has been applied to all pairs of adjacent electrodes (in both boreholes).

Carbon capture and storage (CCS) has gained widespread recognition as an effective means of mitigating carbon dioxide (CO₂) emissions amid the escalating global climate crisis. During the process of storing CO₂ in underground reservoirs, the implementation of robust monitoring measures to track changes in the distribution of underground CO₂ can facilitate the evaluation of the effectiveness and safety of carbon sequestration. Cross-borehole electrical resistivity tomography (ERT), as a form of electromagnetic method, exhibits high sensitivity to deeper pore fluids and rock structures (Daily, 1991), which offers advantages such as ease of implementation, nondestructiveness, cost-effectiveness, and high resolution (Binley, 2005); moreover, ERT provides valuable spatiotemporal information on changes within the underground storage area (Falcon-Suarez, 2017). Consequently, it has found extensive applications in diverse domains, including groundwater resource investigation (Chen, 2022), mineral resources exploration (Prakash, 2022), and geological disaster prediction (Adhikari, 2016).

Currently, significant progress in ERT has been achieved in CO₂ storage projects (Carrigan, 2013). For instance, the Ketzin pilot CO₂ project in Germany demonstrated that CO₂ injection generated a substantial electrical signal in the downhole electrode, which facilitated the real-time monitoring of the downhole potential electrode (Schmidt-Hattenberger, 2013); moreover, the joint inversion of seismic and resistivity tomography reveals an approximately twofold increase in resistivity resulting from CO₂ injection (Wagner, 2018). The permanently installed monitoring electrodes in wells demonstrate the effective detection of minute amounts of injected CO₂ in the CaMI project in Canada (Li, 2022). Likewise, during the Svelvik CO₂ Field Lab experiment, four electrodes were placed at a depth of 100 m, facilitating the successful monitoring of the impacts of CO₂ injection on formation saturation and pore pressure (Raab, 2020).

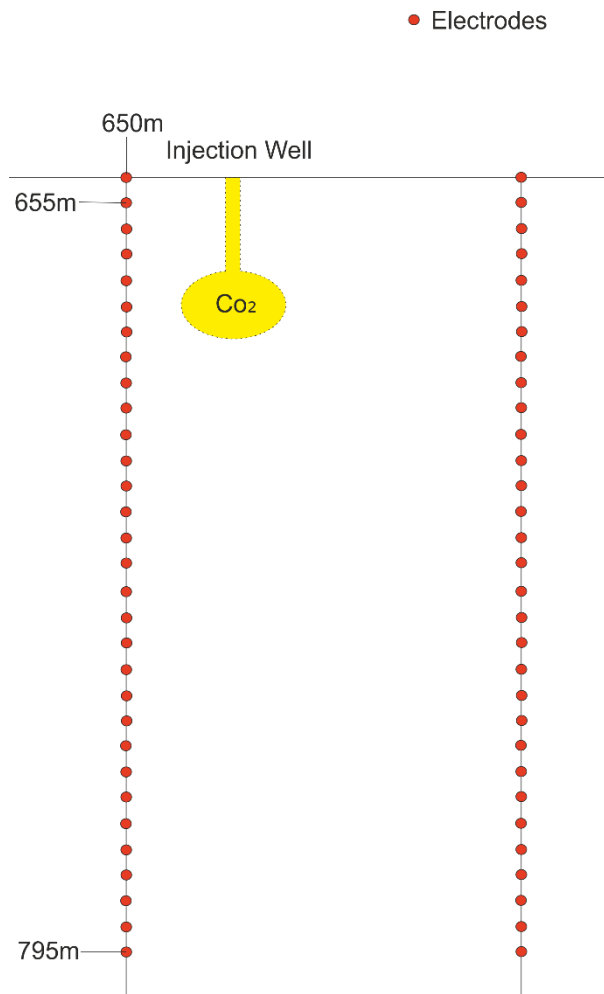


Figure 1. 9 Cross Well ERT Acquisition

1.2.4.1 Application of cross well ERT

- Monitoring Carbon Dioxide Sequestration using Electrical Resistance Tomography
- Cross Well Electrical Resistivity Tomography (ERT) Monitoring for Landslides

Chapter-2

Processing and Forward Modelling

2.1 Processing of Cross-Well Electrical Resistivity Tomography Data

After acquiring field data, the next step involves converting resistance measurements into their respective apparent resistivities. To ensure the accuracy of the resulting model, the data must be of high quality, and devoid of any noise interference. Processing entails the meticulous removal of such noise and refining the data to extract the desired, usable information.

2.2 Noise in Cross-Well Electrical Data

Electrical resistivity tomography (ERT) surveys are relatively insensitive to urban noise. However, background electrical noise can affect the imaging resolution of ERT surveys.

1. **Wellbore Effects:** The condition of the boreholes and the materials used in the wells can influence the measurements. Irregularities in the wellbore, changes in casing material, or the presence of conductive fluids can affect the resistivity measurements.
2. **Temperature and Pressure Changes:** Variations in temperature and pressure within the subsurface can impact the resistivity measurements. These changes may be related to seasonal variations, pumping activities, or other environmental factors.
3. **Instrumentation Noise:** Noise originating from the measurement equipment itself, including the electrodes and cables used, can introduce errors. Regular calibration and maintenance of the instruments are essential to minimize this type of noise.

2.3 Noise Removal

Before proceeding with data inversion for cross-well applications, it's essential to conduct a thorough noise analysis.

Outlined below are several recommended processing steps tailored for cross-well scenarios:

- Establish a suitable range of apparent resistivities pertinent to the specific geological setting and operational conditions, and retain data falling within this range.
- Exclude data points exhibiting excessively large standard deviations, as these may indicate potential noise contamination.
- Discard data associated with very low current values, as such readings can be indicative of noise or poor signal quality.

- Eliminate data points linked to negative or extremely small voltage readings, which could skew the accuracy of the subsequent inversion.
- Implement manual inspection and removal of any evidently erroneous or unreliable data points identified through rigorous scrutiny.

2.3 Forward modelling

2.3.1 Finite element methods (FEM)

The Finite Element Method (FEM) is well-suited for simulating resistivity distribution in the subsurface, as it can handle complex geometries and heterogeneous media effectively (Bing, 2001). FEM are commonly used to model electrical resistance measurements in 2D cross-well configurations. Generating a finite element mesh (FEM) is a crucial step in this process. In 2D ERT modeling, rectangular or triangular elements are typically employed. However, for cross-well applications, triangular elements are often preferred due to their ability to better capture the geometry of the subsurface between the boreholes.

This study utilizes triangular mesh elements to provide flexibility in mesh refinement, particularly around small-scale features such as fractures, boreholes, and electrodes. Additionally, triangular elements facilitate the incorporation of topography into the model. This approach enhances the accuracy of the electrical resistance measurements in the cross-well setup.

Importance of Unstructured Triangle Meshes:

We found a better way to organize our data called unstructured triangle meshes. They help us describe complex shapes more easily and refine our calculations where needed. By using these meshes, we can make our calculations much more accurate while using fewer resources.

2.3.2 Calculation of the total potential

Control Equation: The fundamental equation governing the resistivity model involves the relationship between current density (J), electric field strength (E), electrical conductivity (σ), and electric potential (u). This relationship is expressed as:

$$J = \sigma E \quad (2.1)$$

$$E = -\nabla U \quad (2.2)$$

$$\nabla \cdot J = \partial t / \partial e \quad (2.3)$$

$$\nabla \cdot (\sigma \nabla u) = -2I \cdot \delta(A) \quad (2.4)$$

Here, J represents the current density (A/m²), E denotes the electric field strength (V/m), σ is the electrical conductivity (S/m), u is the electric potential (V), and q represents the amount of charge flowing into the closed surface (Q).

Boundary Condition: The boundary conditions play a crucial role in defining the behavior of the electric potential at the boundaries of the modeling domain. These conditions are described as follows:

$$\frac{\partial u}{\partial n} = 0, \text{ for } \in \in_0^s \quad (2.5)$$

$$\frac{\partial u}{\partial n} + \frac{\cos(r,n)u}{r} = 0, \text{ for } \in \in_0^\infty \quad (2.6)$$

$$u_1 = u_2, \text{ for } \in \in_0 \quad (2.7)$$

Here, \in_0^s represents the boundary between the air and the formation, \in_0^∞ represents the boundary at infinity, and \in_0 is the interface between two media. n indicates the outer normal direction of the boundary, and r is the distance from the point source to the boundary. These boundary conditions ensure the appropriate behaviour of the electric potential at different boundary interfaces within the modeling domain.

2.3.3 Mesh generation and refinement

Mesh generation and refinement are crucial steps in conducting 2D cross-well electrical resistivity tomography (ERT). Initially, the modeling domain is partitioned based on the layout of electrodes, which are often fixed as nodes. However, additional refinement is necessary to address the singular potential at the electrode positions.

Traditional approaches in ERT often utilize block-oriented grids for both finite difference (FD) and finite element (FE) calculations. These grids introduce grid lines between electrodes to minimize calculation errors. By adding two to four additional grid lines between electrodes, the relative error in calculations is typically reduced to around 4% for pole-pole configurations. However, for configurations with large geometric factors, such as dipole-dipole setups, further refinement is needed to reduce error amplification.

In 2D cross-well ERT, the use of unstructured meshes offers significant advantages. These meshes allow for refinement within specific regions, enabling fine meshing in areas with varying potential gradients near electrodes, while cell sizes grow towards the boundaries of the modeling domain.

Mesh refinement strategies can be categorized as a-posteriori or a-priori. In a-posteriori refinement, discretization depends on error estimation during the solution process. In contrast, a-priori refinement involves introducing information in advance, typically based on known critical regions. The a-priori approach is often preferred as it enables the enforcement of a locally fine mesh by adding supporting nodes during the mesh generation process.

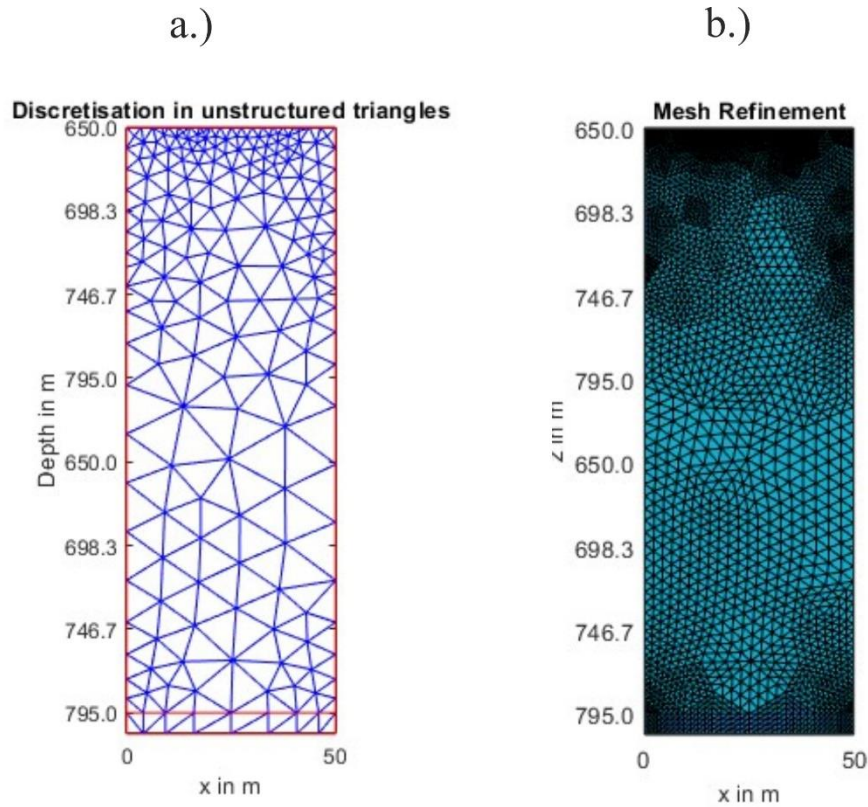


Figure 2. 1 a.) Discretisation in unstructured triangles b.) Mesh Refinement

2.4 Models

2.4.1 Model 1

In our study, we employed a synthetic model representing a homogeneous medium with a resistivity of 200 ohm-m. To simulate the presence of CO₂, we introduced a body with a resistivity of 100 ohm-m into this medium. The body is defined by a polygonal shape with vertices at coordinates 15, 16, 17, 26, 27, and 28.

Our objective was to mimic CO₂ injection from a well, with the gradual spread of CO₂ within the subsurface medium. To achieve this, we incrementally adjusted the size or extent of the body at different time intervals, representing the progression of CO₂ injection.

At time t_1 , the vertices defining the body were located at coordinates 15, 16, 17, 26, 27, and 28 with the resistivity of the medium remaining at 100 ohm-m and the resistivity of the body was 10 ohm-m.

At time t_2 , the vertices shifted to coordinates 12, 13, 14, 30, 31, and 32, with the resistivity of the medium remaining at 100 ohm-m and the resistivity of the body adjusted to 15.85 ohm-m.

At time t_3 , the vertices further changed to coordinates 10, 11, 12, 34, 35, and 36, while the resistivity of the medium remained constant at 100 ohm-m, and the resistivity of the body increased to 25.12 ohm-m.

Finally, at time t_4 , the vertices shifted to coordinates 10, 11, 12, 35, 36, and 37, with the resistivity of the medium staying at 100 ohm-m, and the resistivity of the body increasing to 39.81 ohm-m.

These adjustments represent the dynamic nature of CO₂ injection and spread within the subsurface medium over time, allowing us to study its impact and behavior in a controlled environment.

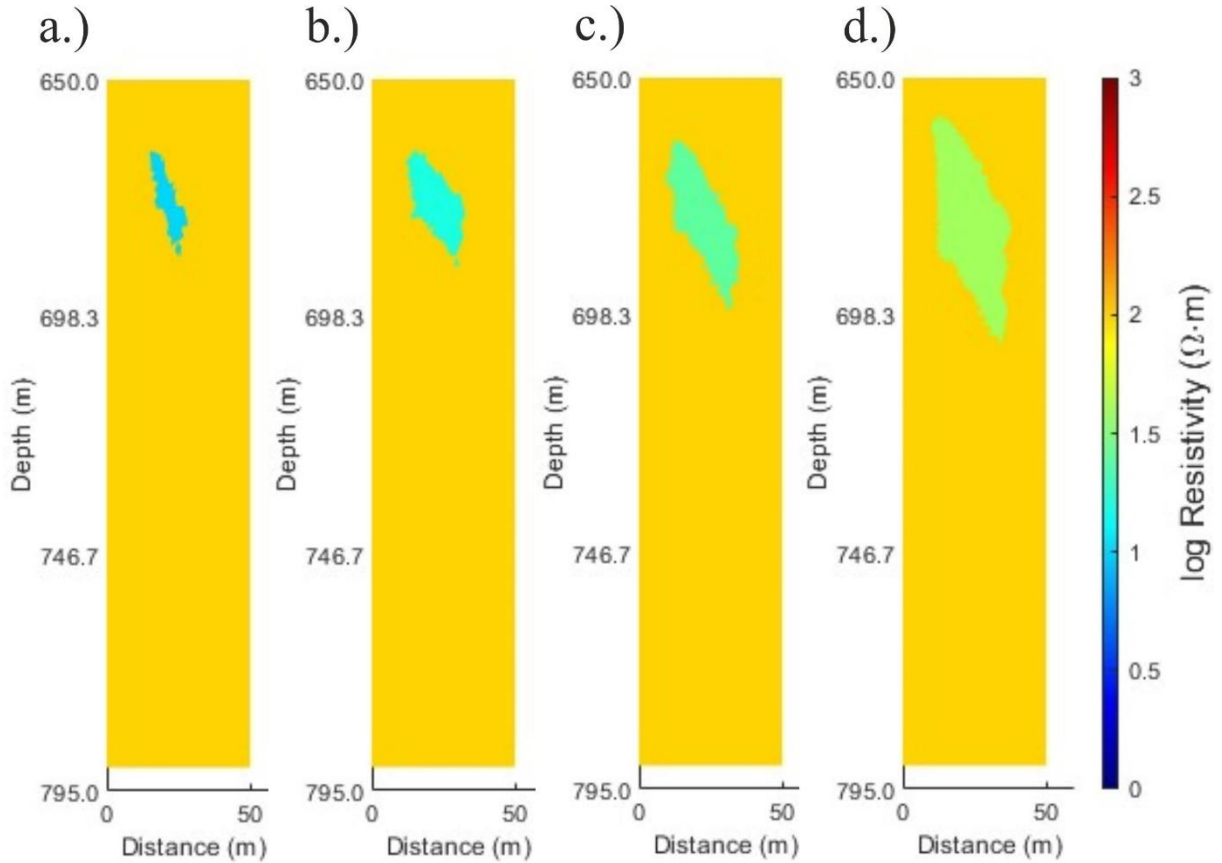


Figure 2. 2 Simulation of CO₂ injection and spread within a homogeneous subsurface medium. The polygon represents the injected CO₂ body, with changing resistivity values over time (t_1 - t_4). The coordinates of the body's vertices and the resistivity of the medium and body are detailed at each time step. This dynamic model provides insights into the behavior and impact of CO₂ injection in a controlled environment

2.4.2 Model 2

In our study, we utilized a synthetic model representing a heterogeneous medium with varying resistivity values. At t_1 , the resistivity values of the medium were as follows: the first layer had a resistivity of approximately 125.89 ohm-m, the second layer had a resistivity of approximately 125.89 ohm-m, and the resistivities of the third and fourth layers were 100 ohm-m and 100 ohm-m, respectively.

To simulate CO₂ injection and spread within this heterogeneous medium, we introduced a body with a resistivity of 10 ohm-m. The body was defined by a polygonal shape with vertices at coordinates 15, 16, 17, 26, 27, and 28.

At t_2 , the vertices shifted to coordinates 12, 13, 14, 30, 31, and 32. The resistivity values of the medium were updated to approximately 158.49 ohm-m for the first layer, 158.49 ohm-m for the second layer, and remained constant at 100 ohm-m for the third and fourth layers. The resistivity of the body was adjusted to 6.3095 ohm-m.

At t_3 , the vertices shifted to coordinates 10,11,12,34,35 and 36. The resistivity values of the medium were updated to approximately 199.53 ohm-m for the first layer, 199.53199.53 ohm-m for the second layer, and remained constant at 100 ohm-m for the third and fourth layers. The resistivity of the body was adjusted to approximately 6.3095 ohm-m.

At t_4 , the vertices shifted to coordinates 10,11,12,34,35 and 36. The resistivity values of the medium were updated to approximately 223.87 ohm-m for the first layer, 223.87223.87 ohm-m for the second layer, and remained constant at 100100 ohm-m for the third and fourth layers. The resistivity of the body was adjusted to approximately 4.4668 ohm-m.

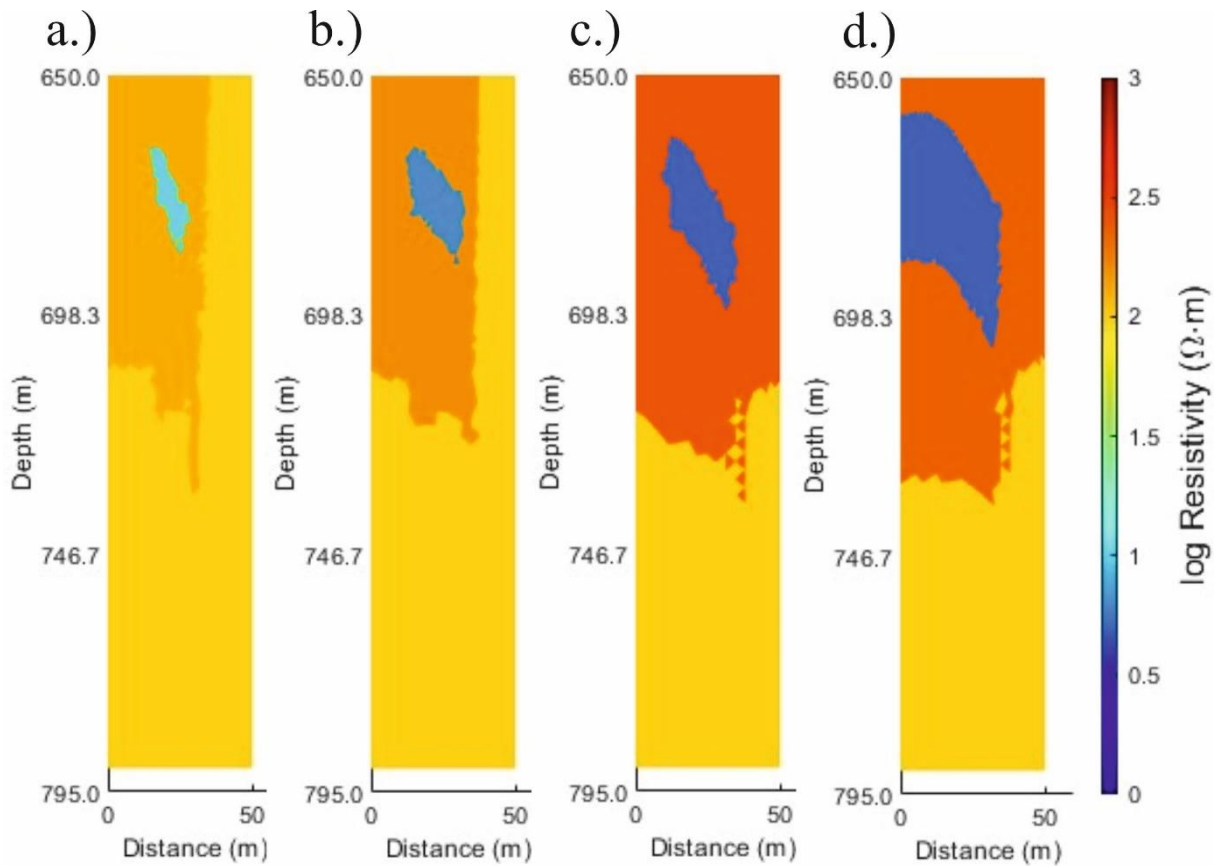


Figure 2. 3 Simulation of CO₂ injection and spread within a heterogeneous subsurface. The polygon represents injected CO₂, with changing resistivity over time (t_1 - t_4). Varying colors indicate the heterogeneous nature of the subsurface. Insights gained from this model aid in understanding CO₂ behaviour in realistic geological settings

Chapter-3

Inversion and Model Resolution

3.1 Inversion

Cross-well Electrical Resistivity Tomography (ERT) inversion is a process employed to reconstruct the distribution of subsurface electrical resistivity or conductivity by analysing measurements obtained from electrodes placed in different wells. In the case of ERT, these measurements typically involve the apparent resistivity data.

Mathematically, the subsurface can be represented by a set of parameters, and the inversion process aims to estimate these parameters based on the recorded measurements. This computationally intensive process often results in a "recovered" or "constructed" model obtained through numerical techniques.

One critical step in ERT inversion is assessing whether the model adequately reproduces the observed measurements, ensuring that the misfit between observed and predicted data is minimized.

3.2 Inversion of Cross-well ERT Data

While cross-well ERT methods provide valuable information about subsurface resistivity or conductivity structures, they alone cannot directly infer the subsurface geology. To obtain an accurate spatial conductivity distribution, specific inversion algorithms and techniques are necessary. However, the inversion of cross-well ERT data poses challenges due to its under-determined nature and the potential presence of significant data errors, rendering the problem generally ill-posed.

Typically, inversion is carried out iteratively, with the process terminating when the root mean square error approaches a value close to zero. To perform the inversion, a parameter mesh is created to define the cells whose resistivities are to be determined. In this study, a triangular mesh is utilized, chosen based on computational considerations and requirements.

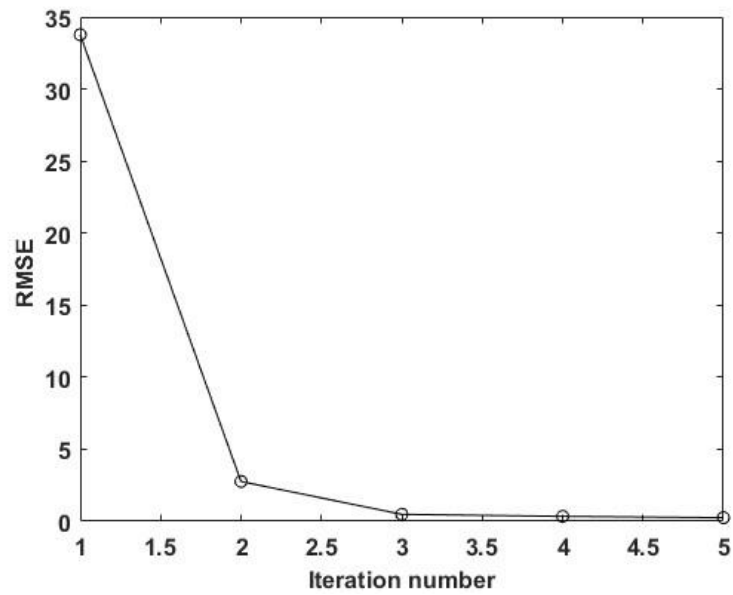


Figure 3. 1 Convergence curve of the data error as a function of the iteration number

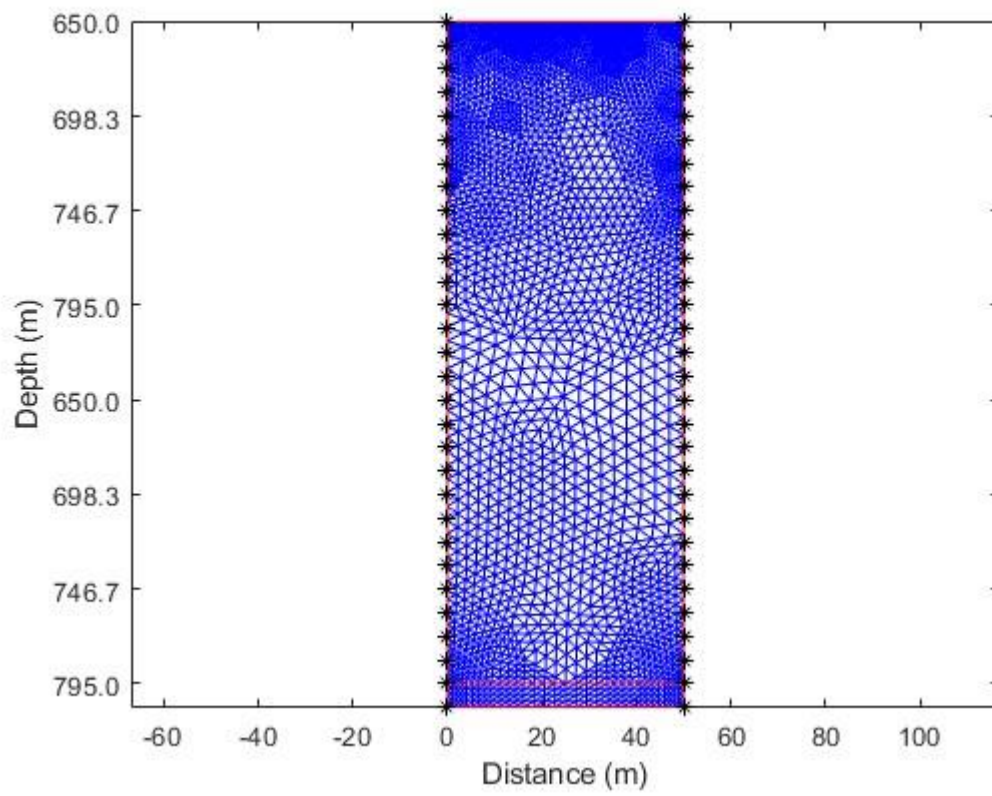


Figure 3. 2 Minimisation of RMS error in successive iterations and parameter Triangular mesh Grid to carry out inversion for individual cells

3.2.1 Choice of Norm

The l_p norm is defined as

$$\|e\|_p^p = \sum_{j=1}^N |e_j|^p. \quad (3.1)$$

The norm proposed by (Eklom, 1987) which is a revised form of the l_p norm is used in this study. The expression for this norm is given below :-

$$l_p(e) = (e^2 + \varepsilon^2)^{p/2} \quad (3.2)$$

Here ε is a positive number. When ε is very small it will approach the l_p norm given in equation 1, for very large ε it behaves like a scaled sum of squares measure.

3.2.2 Minimization of Inverse Problem

We have taken $p=2$ since we are using L-2 Norm. The objective function for the minimization of data misfit along with function model regularization parameter and using Tikhonov parametric function in this study:

Considering s.t. $\phi < \phi^*$,

$$\phi^{\text{total}}(m) = \|W^d(F(m) - d^{\text{obs}})\|_2^2 + \lambda_1 \|\alpha_1 W_s^m(m - m^{\text{ref}})\|_2^2 \quad (3.3)$$

where ϕ^* is the target misfit. The first term corresponds to the data misfit and the second to model regularisation function with weighting matrices W^d and W_s^m . Using (Oldenburg, 1998) the objective function to be minimized can be written as-

$$\phi = [\phi_d\{W^d(F(m) - d^{\text{obs}})\} - \phi^*] + \lambda_1[\phi_{m_1} \times \{\alpha_1 W_s^m(m - m^{\text{ref}})\}] \quad (3.4)$$

Let us assume that model at k th iteration is m^k , predicted data are d^k for this model and model update at $k+1$ th iteration is $m^{k+1} = m^k + \Delta m^{k+1}$. Writing equation 2 for m^{k+1} using Taylor's series expansion of $F(m)$ and discarding the second and higher order derivatives result in

$$\begin{aligned} \phi(m^{k+1}) = & \left[\phi_d \left\{ W^d \left(\left(F(m^k) + \frac{\partial F}{\partial m} \Delta m^{k+1} \right) - d^{\text{obs}} \right) \right\} - \phi^* \right] \\ & + \lambda_1 [\alpha_1 \phi_{m_1} \{ W_s^m (m^k + \Delta m^{k+1} - m^{\text{ref}}) \}] \end{aligned} \quad (3.5)$$

Writing the sensitivity matrix $\frac{\partial F}{\partial m}$ as J^k -

$$\begin{aligned}\phi(m^{k+1}) = & [\phi_d\{W^d(d^k + J^k \Delta m^{k+1} - d^{obs})\} - \phi^*] \\ & + \lambda_1 [\alpha_1 \phi_{m_1}\{W_s^m(m^k + \Delta m^{k+1} - m^{ref})\}] \end{aligned} \quad (3.6)$$

Now differentiating this equation w.r.t Δm^{k+1} and assuming ,

$$L_{j=(d,s)} = \begin{cases} W^d(d^k + J^k \Delta m^{k+1} - d^{obs}) \\ W_s^m(m^k + \Delta m^{k+1} - m^{ref}) \end{cases} \quad (3.7)$$

will lead to

$$\frac{\partial \phi}{\partial (\Delta m^{k+1})} = \left[\frac{\partial [\phi_d\{L_d\} - \phi^*]}{\partial (\Delta m^{k+1})} + \lambda_1 \frac{\partial [\alpha_1 \phi_{m_1}\{L_s\}]}{\partial (\Delta m^{k+1})} \right] \quad (3.8)$$

Differentiating the right side of equation 2.8 by the chain rule and putting the value of L_d and L_s from equation 2.7 result in

$$\frac{\partial [\phi_d\{L_d\} - \phi^*]}{\partial (\Delta m^{k+1})} = \frac{\partial \phi_d(L_d)}{\partial (L_d)} \frac{\partial (W^d(d^k + J^k \Delta m^{k+1} - d^{obs}))}{\partial (\Delta m^{k+1})},$$

$$\frac{\partial [\phi_d\{L_d\} - \phi^*]}{\partial (\Delta m^{k+1})} = (J^k)^T (W^d)^T \frac{\partial \phi_d(L_d)}{\partial (L_d)},$$

where superscript T is the transpose of the matrix. Similarly, putting the values of all the differential terms in equation 2.8 results in

$$\frac{\partial [\phi_d\{L_d\} - \phi^*]}{\partial (\Delta m^{k+1})} = (J^k)^T (W^d)^T \frac{\partial \phi_d(L_d)}{\partial (L_d)}, \quad (3.9)$$

Differential equation 2.2 with result in -

$$\frac{\partial \ell(e)}{\partial e} = p(e^2 + \varepsilon^2)^{\frac{p}{2}-1} e \quad (3.10)$$

Following the analogy of equation 2.10 and putting $p=2$,

$$\frac{\partial \phi_d(L_d)}{\partial (L_d)} = p((L_d)^2 + \varepsilon^2)^{\frac{p}{2}-1} (L_d) \quad (3.11)$$

$$\frac{\partial \phi_d(L_d)}{\partial (L_d)} = 2L_d \quad (3.12)$$

Similarly ,

$$\frac{\partial \phi_{m_1}(L_s)}{\partial (L_s)} = 2L_s \quad (3.13)$$

Now putting the values from equations 2.7, 2.12 and 2.13 in equation 2.9 and equating it to zero results in,

$$\left[(J^k)^T (W^d)^T R_d W^d (d^k + J^k \Delta m^{k+1} - d^{obs}) + \lambda_1 (\alpha_1 (W_s^m)^T R_s W_s^m (m^k + \Delta m^{k+1} - m^{ref})) \right] = 0 \quad (3.14)$$

Simplifying for (k+1)th iteration,

$$\Delta m^{k+1} = [(J^k)^T (W^d)^T W^d J^k + \lambda_1 \alpha_1 (W_s^m)^T W_s^m]^{-1} \times \left[(J^k)^T (W^d)^T W^d (d^{obs} - d^k) - \lambda_1 (\alpha_1 (W_s^m)^T W_s^m (m^k - m^{ref})) \right] \quad (3.15)$$

3.4 Cross Well ERT Inversion Workflow

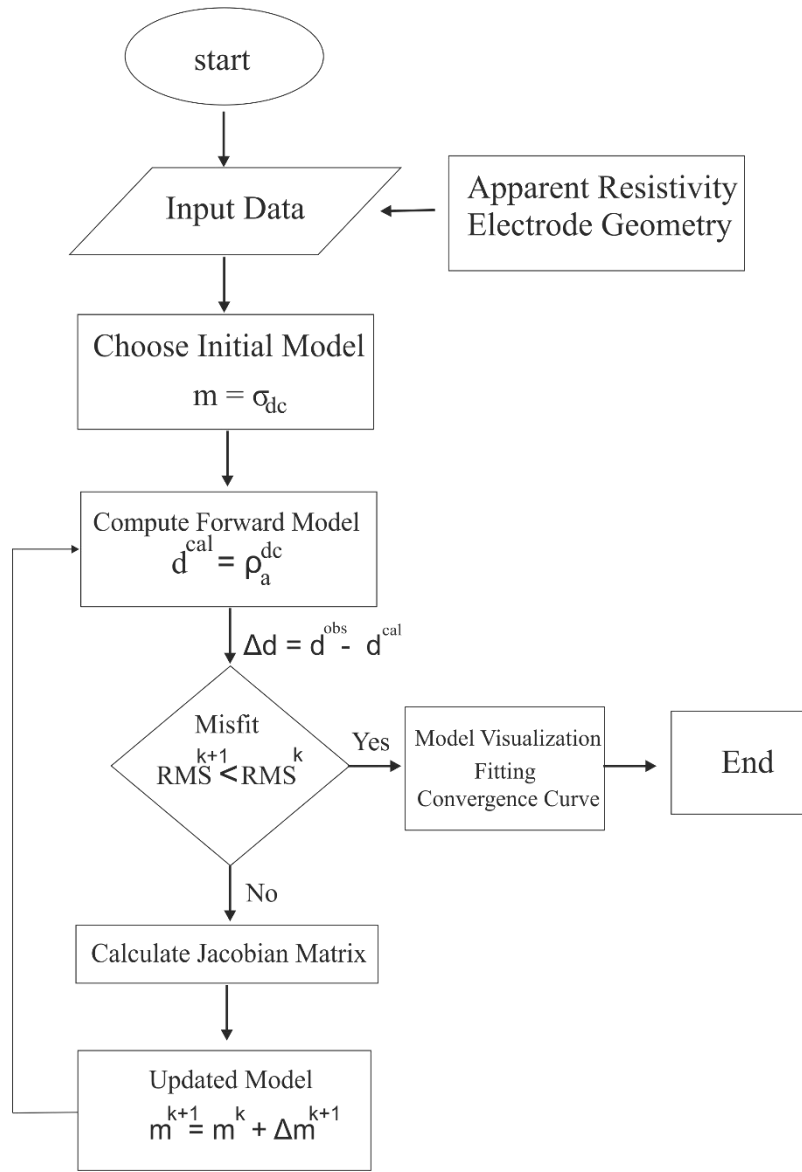


Figure 3. 3 Flow chart of the inversion procedure

3.5 Model Resolution Matrix

The model resolution matrix plays a crucial role in understanding the relationship between the estimated model and the true model in inverse problems. Essentially, it quantifies how accurately the estimated model represents the true model.

$$m^{est.} = G^{-g} d^{true} \quad (3.16)$$

$$m^{est.} = G^{-g} G m^{true} \quad (3.17)$$

$$m^{est.} = R m^{true} \quad (3.18)$$

Given equations (3.16) and (3.17) from the context, where $m^{est.}$ represents the estimated model, m^{true} represents the true model, and G is the data kernel or forward model matrix, we derive the expression for the model resolution matrix $R=G^{-g}G$ as in equation (3.18). For the case of under-determined problem as in the case of DC resistivity problems, the generalised inverse can be written as –

$$G^{-g} = G^T (GG^T)^{-1} \quad (3.19)$$

Using Eq 3.17 , we can write model resolution matrix R as,

$$R = G^T (GG^T)^{-1} G \quad (3.20)$$

Considering J as (N*M) Jacobian Matrix and C as (M*M) smoothing matrix, we can rewrite the model resolution matrix R as follows (Menke, 1989)

$$R = (J^T w_d^T w_d A + \alpha C^T C)^{-1} A^T w_d^T w_d J$$

3.6 Model Resolution Analysis

The model resolution matrix, denoted as R, serves as a tool for evaluating the quality of a model's resolution (e.g., as discussed by (Alumbaugh, 2000), and by (Candansayar, 2008)). By examining the diagonal elements of this matrix, we can establish a parameter indicating the level of resolution achieved by the data. Additionally, the Dirichlet Spread Function comes into play to quantify the disparity between the actual model resolution matrix R and an ideal resolution matrix, typically represented as an identity matrix. We have considered different synthetic model to analysis the model resolution

Chapter 4

Result

In this chapter, we present the outcomes of the inversion process and the analysis of model resolution discussed in Chapter 3. The results provide insights into the effectiveness of the cross-well Electrical Resistivity Tomography (ERT) method in characterizing subsurface properties and detecting anomalies such as CO₂ injection.

4.1 Inversion Results

The inversion results provide crucial insights into the spatial distribution of subsurface electrical resistivity or conductivity, offering a detailed view of the underground structures and fluid dynamics. Here, we analyze two synthetic models first one is homogeneous and the second one is heterogeneous and we make these models like we are injecting the CO₂ into the subsurface.

4.1.1 Model 1

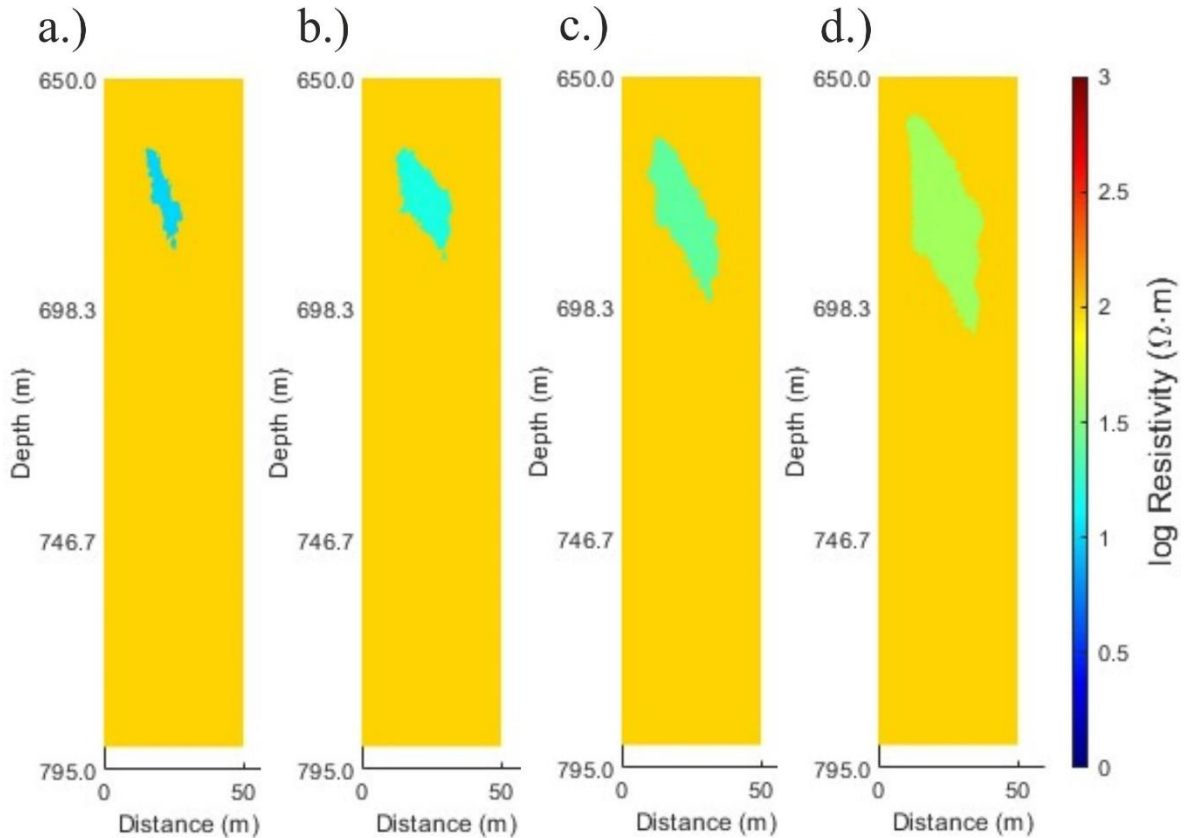


Figure 4. 1 Simulation of CO₂ injection and spread within a homogeneous subsurface medium. The polygon represents the injected CO₂ body, with changing resistivity values over time (t1-t4). The coordinates of the body's vertices and the resistivity of the medium and body are

detailed at each time step. This dynamic model provides insights into the behavior and impact of CO₂ injection in a controlled environment

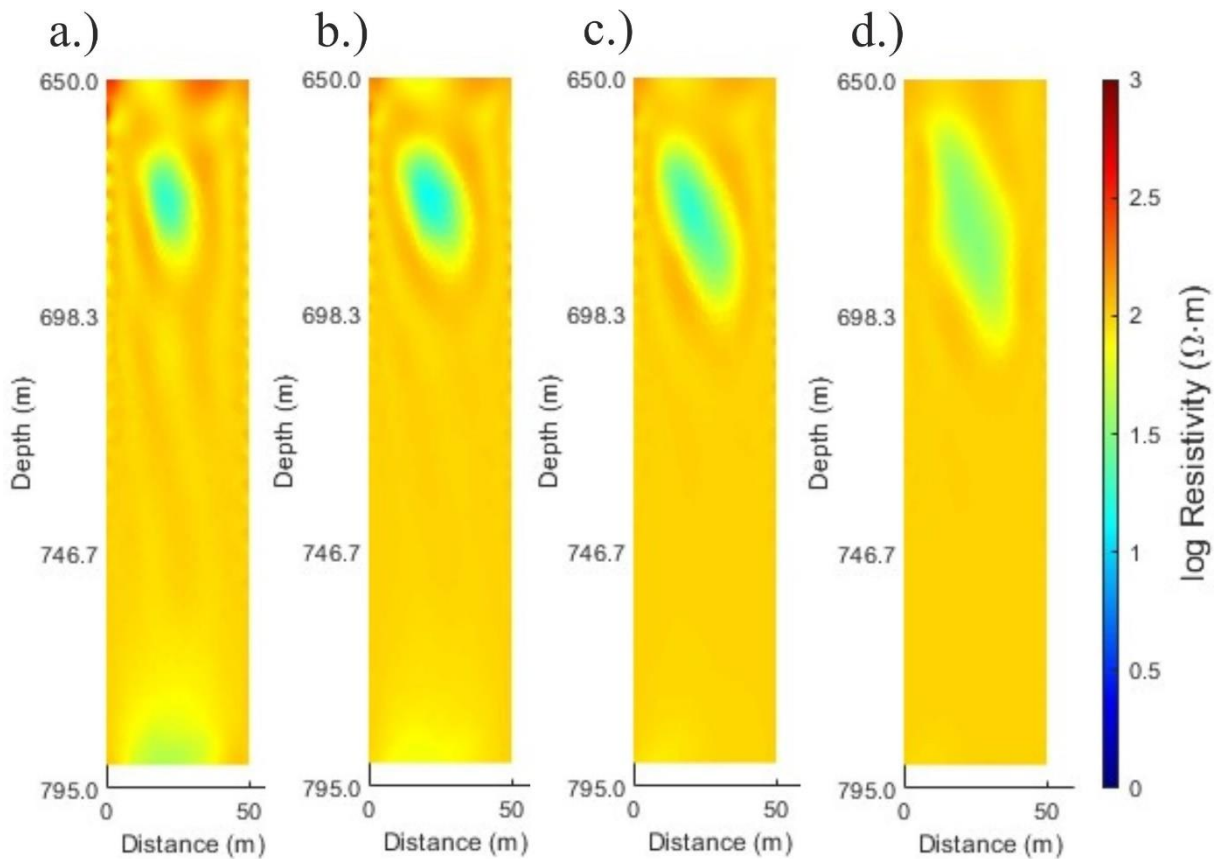


Figure 4. 2 Inverse modeling results show the inferred CO₂ distribution over time (t_1 - t_4), along with the evolving resistivity values of the injected CO₂ body. This visualization provides valuable insights into the spatial distribution and dynamic behavior of injected CO₂ within the subsurface medium

Homogeneous Subsurface Medium

In Figure 4.1, we observe the simulation of CO₂ injection and spread within a homogeneous subsurface medium. The inverted electrical resistivity imaging model (Figure 4.2) captures the temporal evolution of the injected CO₂ body, demonstrating the technique's ability to track fluid migration processes accurately. The consistency between the simulated and inverted models indicates the effectiveness of the inversion process in reconstructing subsurface resistivity distributions in homogeneous environments.

4.1.2 Model 2

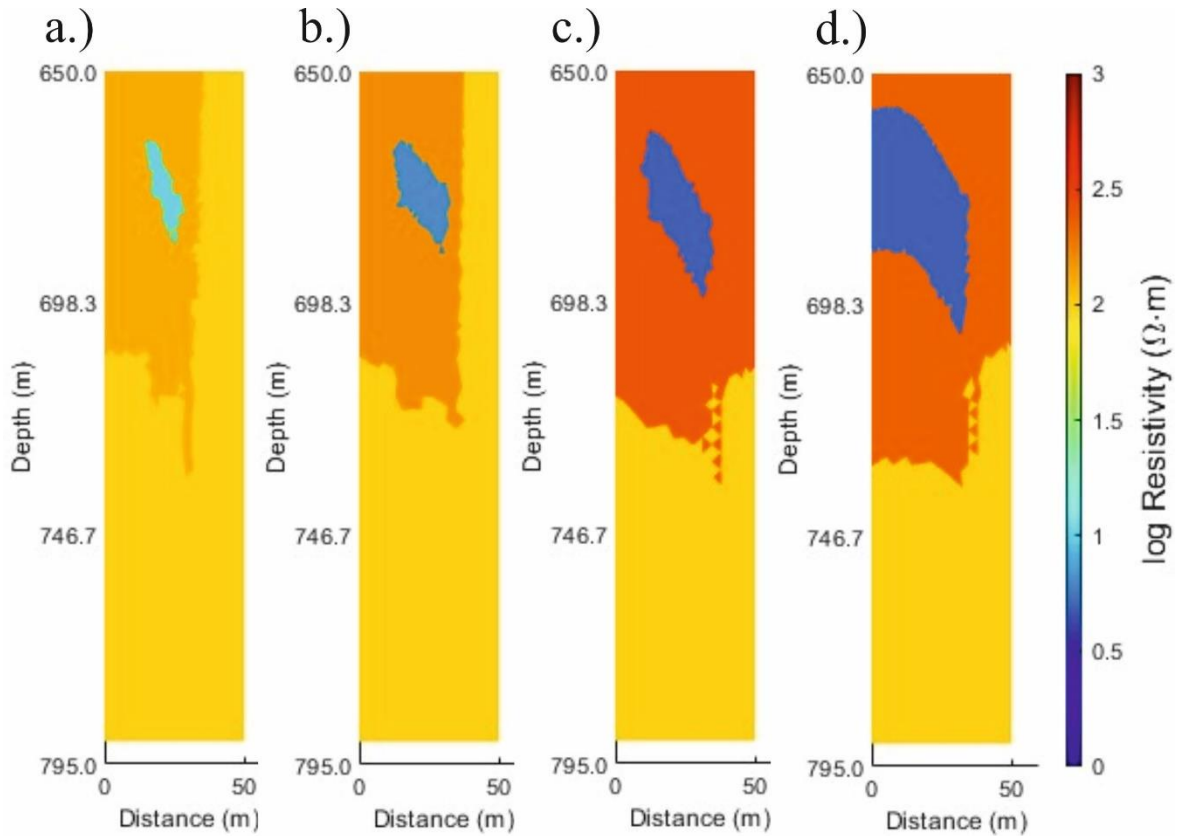


Figure 4. 3 Simulation of CO₂ injection and spread within a heterogeneous subsurface. The polygon represents injected CO₂, with changing resistivity over time (t1-t4). Varying colors indicate the heterogeneous nature of the subsurface. Insights gained from this model aid in understanding CO₂ behaviour in realistic geological settings

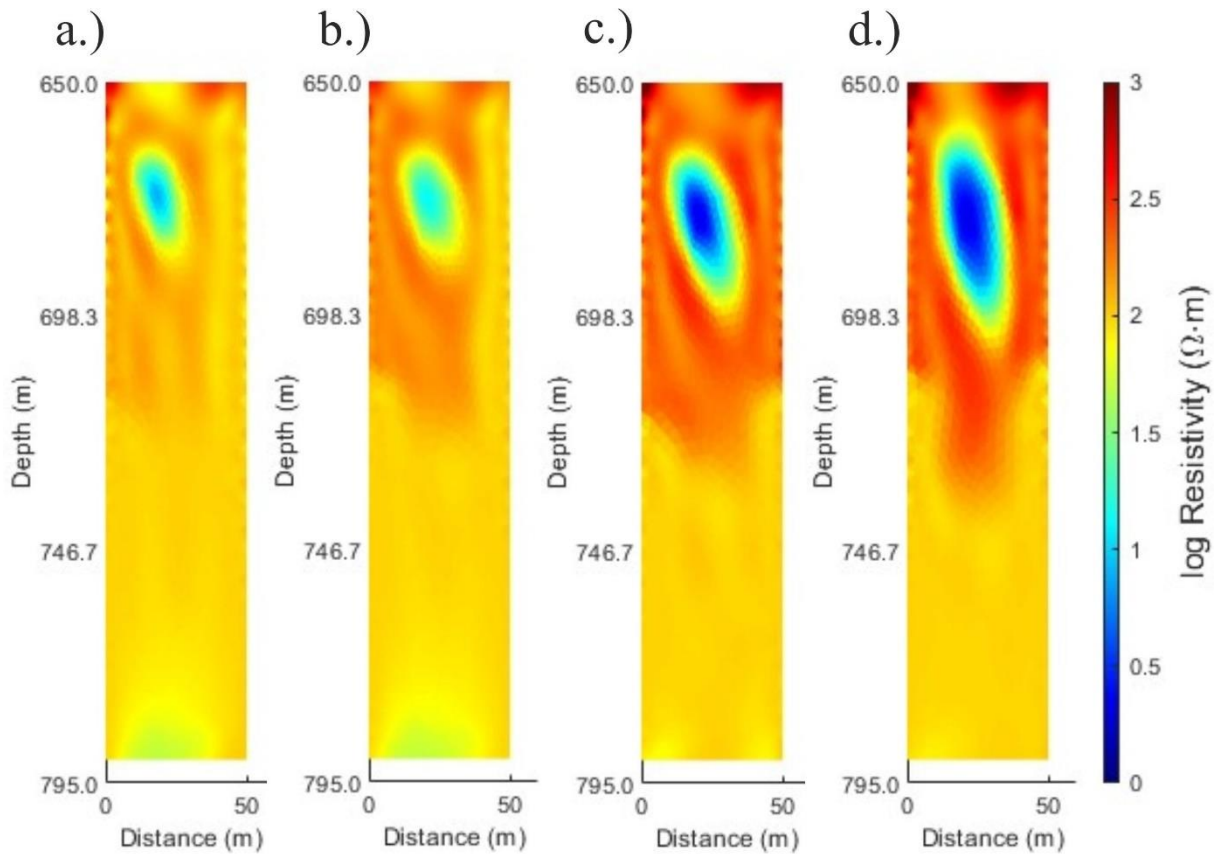


Figure 4. 4 Inverse modeling of CO₂ injection and propagation within a heterogeneous subsurface medium. The inverted results depict the inferred spatial distribution of CO₂ over time (t₁-t₄), considering the dynamic changes in resistivity associated with the injected CO₂ body. The diverse colors reflect the heterogeneity of the subsurface, providing valuable insights into CO₂ behavior within realistic geological formations.

Heterogeneous Subsurface Structures

Figure 4.3 illustrates the simulation of CO₂ injection and spread within a heterogeneous subsurface, presenting additional challenges for subsurface imaging. Despite the complexity introduced by heterogeneities, the inverted electrical resistivity imaging model (Figure 4.4) successfully delineates the spatial distribution of injected CO₂ and captures dynamic changes in subsurface resistivity. The diverse colors in the inverted model reflect the heterogeneity of the subsurface, providing valuable insights into fluid migration behavior in realistic geological settings.

4.1.3 Analysis of Inversion Results

The comparison between simulated and inverted models reveals several important findings:

- **Resolution of Subsurface Features:** The inversion process effectively resolves subsurface features, including fluid plumes and geological structures, even in heterogeneous environments. This capability is crucial for applications such as environmental monitoring and resource management.

- **Quantification of Fluid Dynamics:** The inverted models offer quantitative information about fluid dynamics, enabling the assessment of fluid migration rates and pathways. This information enhances our understanding of subsurface processes and aids in contamination remediation efforts.
- **Characterization of Geological Structures:** The inversion results provide insights into subsurface geological structures, facilitating geological mapping and hydrogeological studies. Accurate delineation of these structures improves our understanding of subsurface properties and behavior.

4.2 Model Resolution Analysis: Evaluating Resolution Quality

The model resolution analysis, based on the resolution matrix denoted as R , serves as a critical tool for assessing the quality of resolution achieved by the inversion process (e.g., as discussed by (Alumbaugh, 2000), and by (Candansayar, 2008)). By examining the diagonal elements of this matrix, we can quantify the level of resolution attained by the inversion model, providing valuable insights into its effectiveness in capturing subsurface features.

4.2.1 Synthetic Model 1

For the cross-well synthetic data analysis, a single-layer model was considered with the following resistivity values:

Background medium: $\rho_1 = 100 \Omega \cdot m$

Anomalous body: $\rho_2 = 10 \Omega \cdot m$

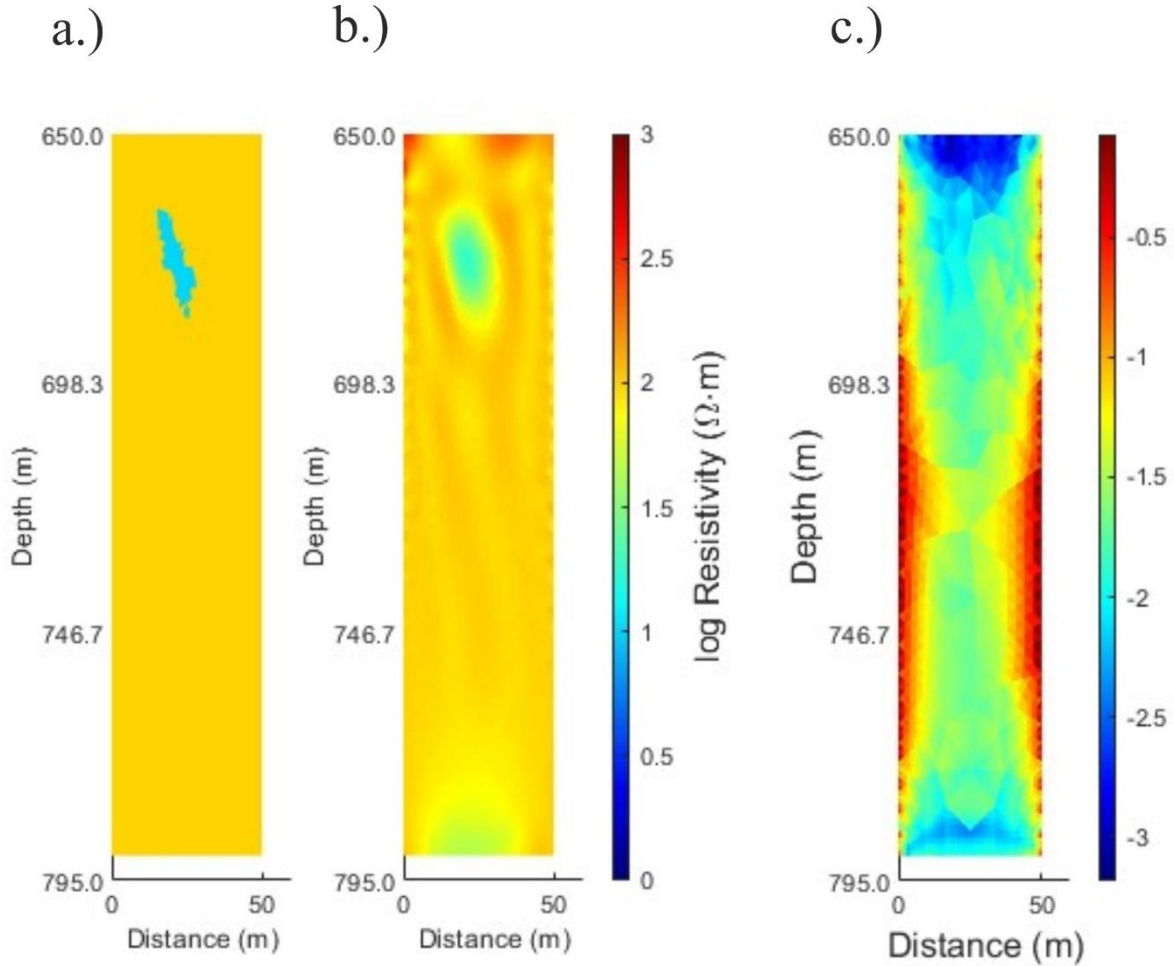


Figure 4. 5 Cross-Well Synthetic Data Analysis: Considering a single layer model with the resistivity values of $\rho_1 = 100 \Omega \cdot m$ for the background medium and $\rho_2 = 10 \Omega \cdot m$ for the anomalous body:(a) Synthetic two-layer model at time t_1 , with the vertices defining the body located at coordinates 15, 16, 17, 26, 27, and 28 while maintaining the resistivity of the medium at $100 \Omega \cdot m$ and the resistivity of the body at $10 \Omega \cdot m$.(b) Inverted electrical resistivity imaging model based on the synthetic data.(c) Model Resolution Matrix depicting the resolution quality of the inverted model.

4.2.2 Synthetic Model 2

For the cross-well synthetic data analysis, a single-layer model was considered with the following resistivity values:

Background medium: $\rho_1 = 100 \Omega \cdot m$

Anomalous body: $\rho_2 = 15.85 \Omega \cdot m$

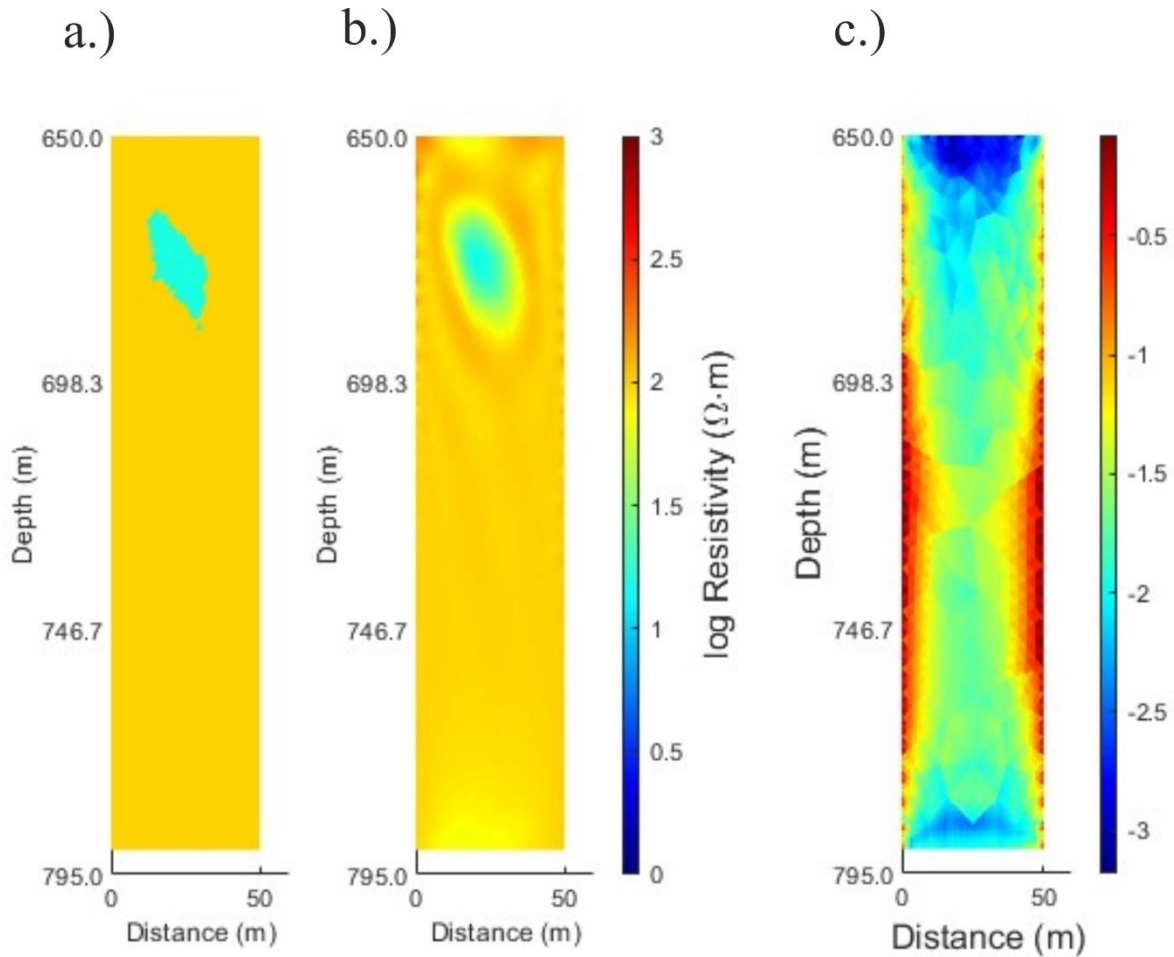


Figure 4. 6 Cross-Well Synthetic Data Analysis: (a) Synthetic two-layer model at time t_2 , with the vertices defining the body shifted to coordinates 12, 13, 14, 30, 31, and 32 while maintaining the resistivity of the medium at $100 \Omega \cdot m$ and adjusting the resistivity of the body to $15.85 \Omega \cdot m$. (b) Inverted electrical resistivity imaging model based on the synthetic data. (c) Model Resolution Matrix depicting the resolution quality of the inverted model.

4.2.3 Synthetic Model 3

For the cross-well synthetic data analysis, a single-layer model was considered with the following resistivity values:

Background medium: $\rho_1 = 100 \Omega \cdot m$

Anomalous body: $\rho_2 = 25.12 \Omega \cdot m$

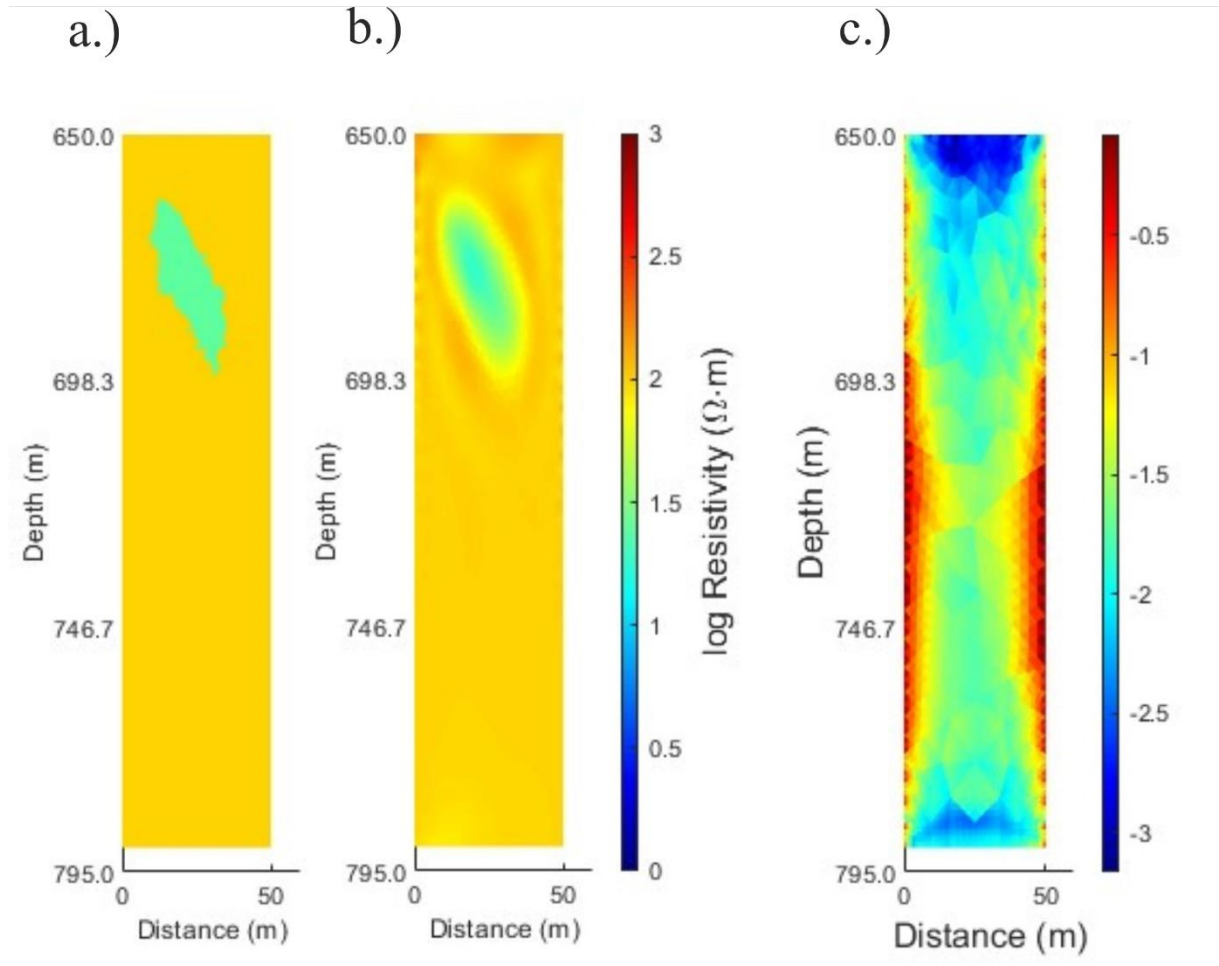


Figure 4. 7 Cross-Well Synthetic Data Analysis: (a) Synthetic two-layer model at time t_2 , with the vertices defining the body shifted to coordinates 10, 11, 12, 34, 35, and 36 while maintaining the resistivity of the medium at 100 $\Omega \cdot m$ and adjusting the resistivity of the body to 25.12 $\Omega \cdot m$. (b) Inverted electrical resistivity imaging model based on the synthetic data. (c) Model Resolution Matrix depicting the resolution quality of the inverted model.

4.2.4 Synthetic Model 4

For the cross-well synthetic data analysis, a single-layer model was considered with the following resistivity values:

Background medium: $\rho_1 = 100 \Omega \cdot m$

Anomalous body: $\rho_2 = 39.81 \Omega \cdot m$

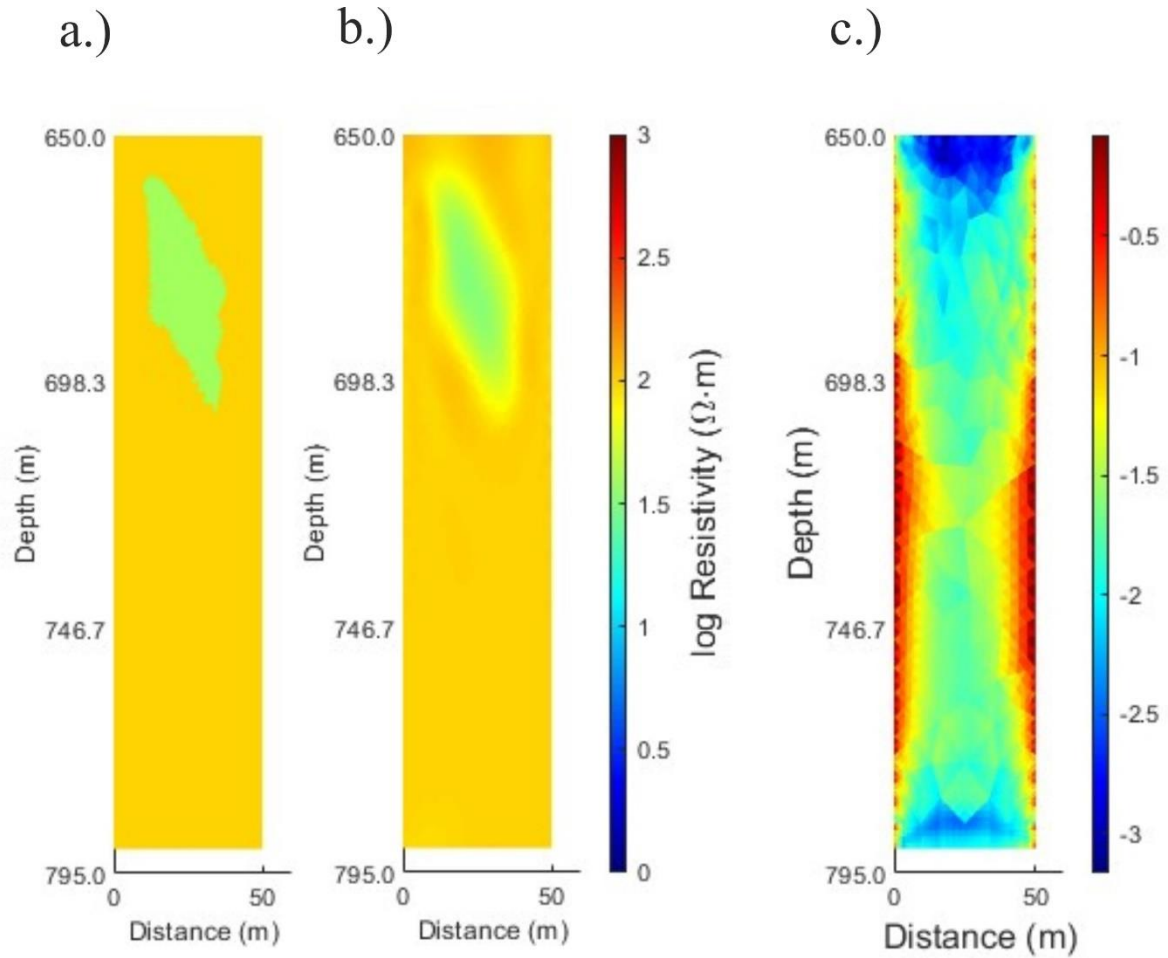


Figure 4. 8 Cross-Well Synthetic Data Analysis: (a) Synthetic two-layer model at time t_2 , with the vertices defining the body shifted to coordinates 10, 11, 12, 35, 36, and 37 while maintaining the resistivity of the medium at $100 \Omega \cdot m$ and adjusting the resistivity of the body to $39.81 \Omega \cdot m$. (b) Inverted electrical resistivity imaging model [$\Omega \cdot m$] based on the synthetic data. (c) Model Resolution Matrix depicting the resolution quality of the inverted model.

4.2.5 Synthetic Model 5

We utilized a synthetic model representing a heterogeneous medium with varying resistivity values. At t_1 , the resistivity values of the medium were as follows: the first layer had a resistivity of approximately 125.89 ohm-m, the second layer had a resistivity of approximately 125.89 ohm-m, and the resistivities of the third and fourth layers were 100 ohm-m and 100 ohm-m, respectively. To simulate CO₂ injection and spread within this heterogeneous medium, we introduced a body with a resistivity of 10 ohm-m. The body was defined by a polygonal shape with vertices at coordinates 15, 16, 17, 26, 27, and 28.

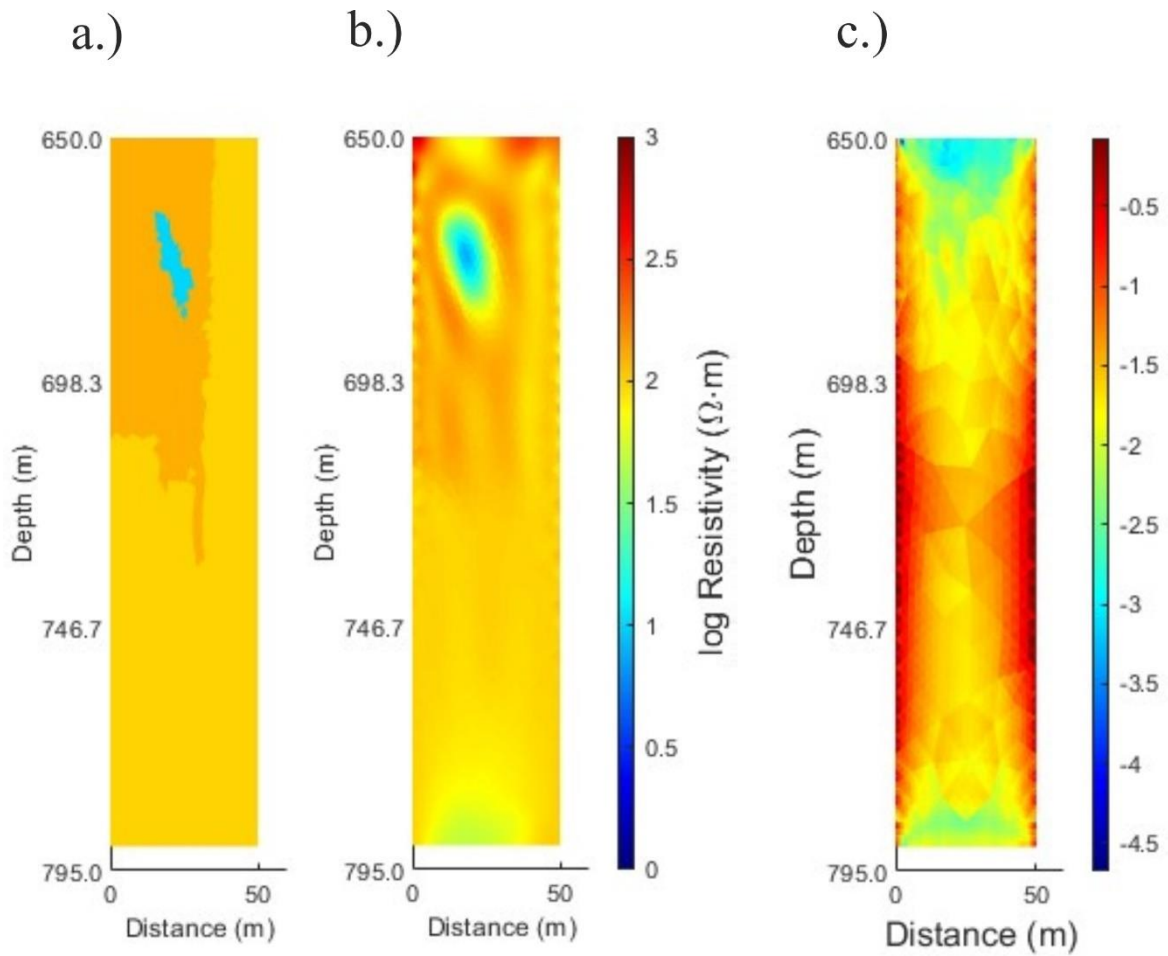


Figure 4. 9 (a) Synthetic model representing a heterogeneous medium characterized by diverse resistivity values. Initially, at time t_1 , the resistivity values of the layers were as follows: approximately 125.89 ohm-m for both the first and second layers, while the third and fourth layers exhibited resistivities of 100 ohm-m each. (b) Inverted electrical resistivity imaging model [Ohm-m] based on the synthetic data. (c) Model Resolution Matrix depicting the resolution quality of the inverted model.

4.2.6 Synthetic Model 6

We utilized a synthetic model representing a heterogeneous medium with varying resistivity values. At t_1 , the resistivity values of the medium were as follows: the first layer had a resistivity of approximately 158.49 ohm-m, the second layer had a resistivity of approximately 158.49 ohm-m, and the resistivities of the third and fourth layers were 100 ohm-m and 100 ohm-m, respectively. To simulate CO₂ injection and spread within this heterogeneous medium, we introduced a body with a resistivity of 6.3095 ohm-m. The body was defined by a polygonal shape with vertices at coordinates 12, 13, 14, 30, 31, and 32.

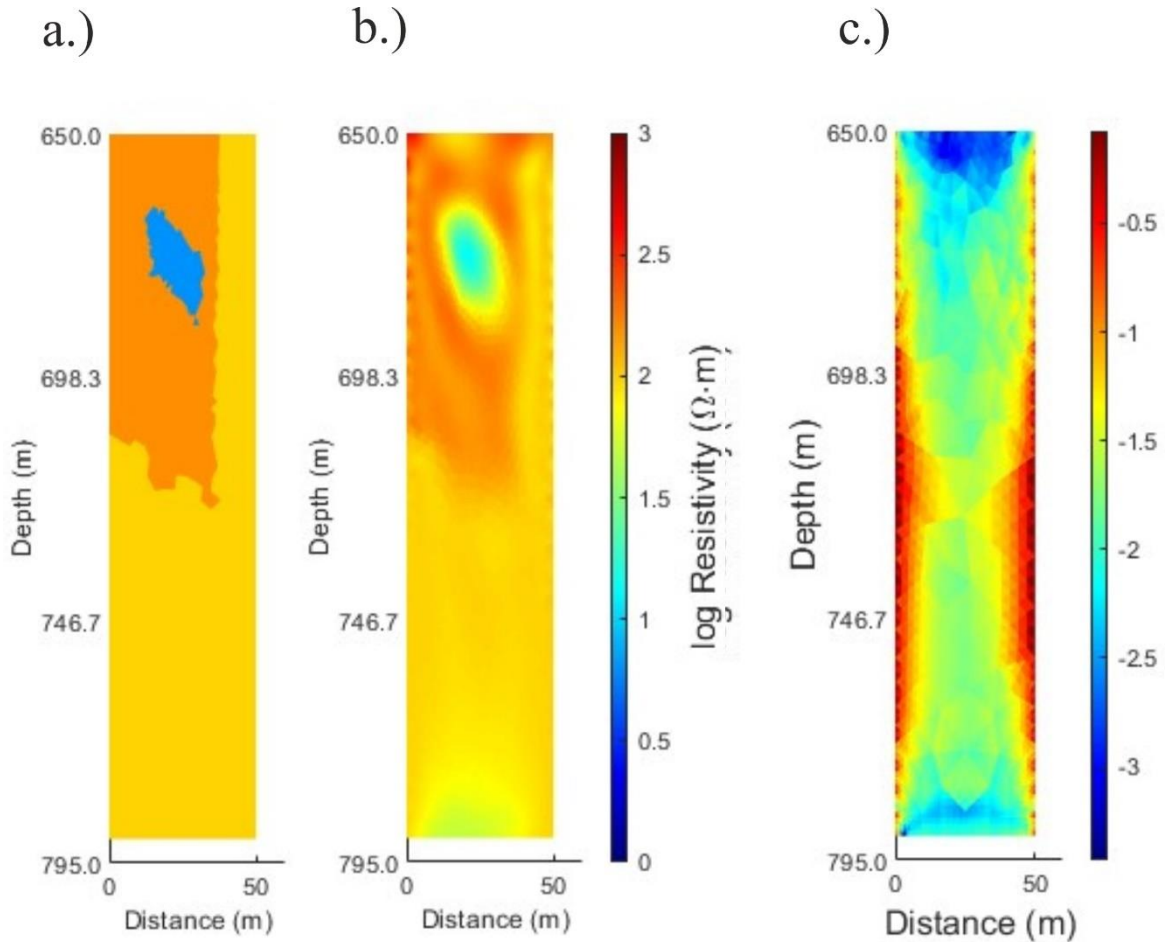


Figure 4. 10 (a) Synthetic model representing a heterogeneous medium characterized by diverse resistivity values. Initially, at time t_1 , the resistivity values of the layers were as follows: approximately 158.49 ohm-m for both the first and second layers, while the third and fourth layers exhibited resistivities of 100 ohm-m each. (b) Inverted electrical resistivity imaging model [Ohm-m] based on the synthetic data. (c) Model Resolution Matrix depicting the resolution quality of the inverted model.

4.2.7 Synthetic Model 7

We utilized a synthetic model representing a heterogeneous medium with varying resistivity values. At t_1 , the resistivity values of the medium were as follows: the first layer had a resistivity of approximately 199.53 ohm-m, the second layer had a resistivity of approximately 199.53 ohm-m, and the resistivities of the third and fourth layers were 100 ohm-m and 100 ohm-m, respectively. To simulate CO₂ injection and spread within this heterogeneous medium, we introduced a body with a resistivity of 5.623 ohm-m. The body was defined by a polygonal shape with vertices at coordinates 10,11,12,34,35 and 36.

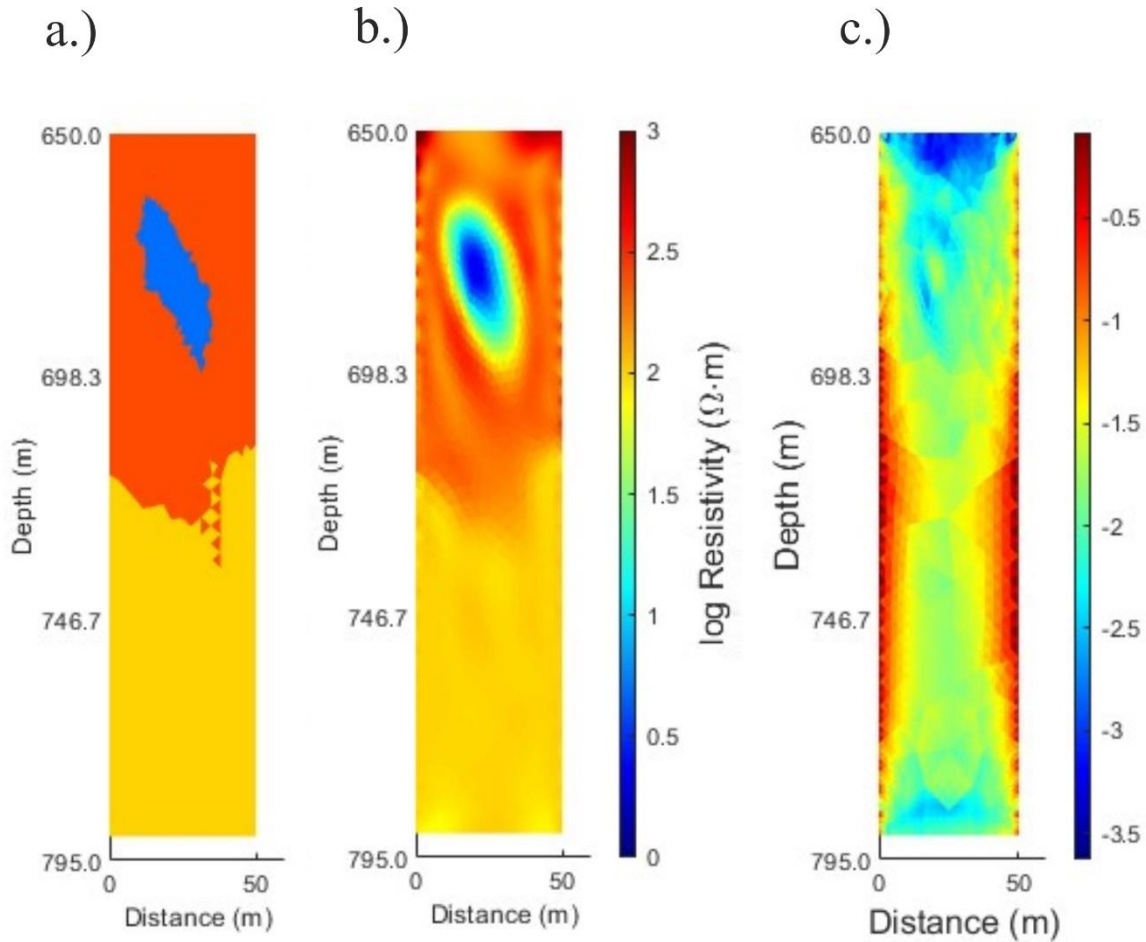


Figure 4. 11 (a) Synthetic model representing a heterogeneous medium characterized by diverse resistivity values. Initially, at time t_1 , the resistivity values of the layers were as follows: approximately 199.53 ohm-m for both the first and second layers, while the third and fourth layers exhibited resistivities of 100 ohm-m each. (b) Inverted electrical resistivity imaging model [Ohm-m] based on the synthetic data. (c) Model Resolution Matrix depicting the resolution quality of the inverted model.

4.2.8 Synthetic Model 8

We utilized a synthetic model representing a heterogeneous medium with varying resistivity values. At t_1 , the resistivity values of the medium were as follows: the first layer had a resistivity of approximately 223.87223.87 ohm-m, the second layer had a resistivity of approximately 223.87223.87 ohm-m, and the resistivities of the third and fourth layers were 100 ohm-m and 100 ohm-m, respectively. To simulate CO₂ injection and spread within this heterogeneous medium, we introduced a body with a resistivity of 4.4668 ohm-m. The body was defined by a polygonal shape with vertices at coordinates 10,11,12,34,35 and 36.

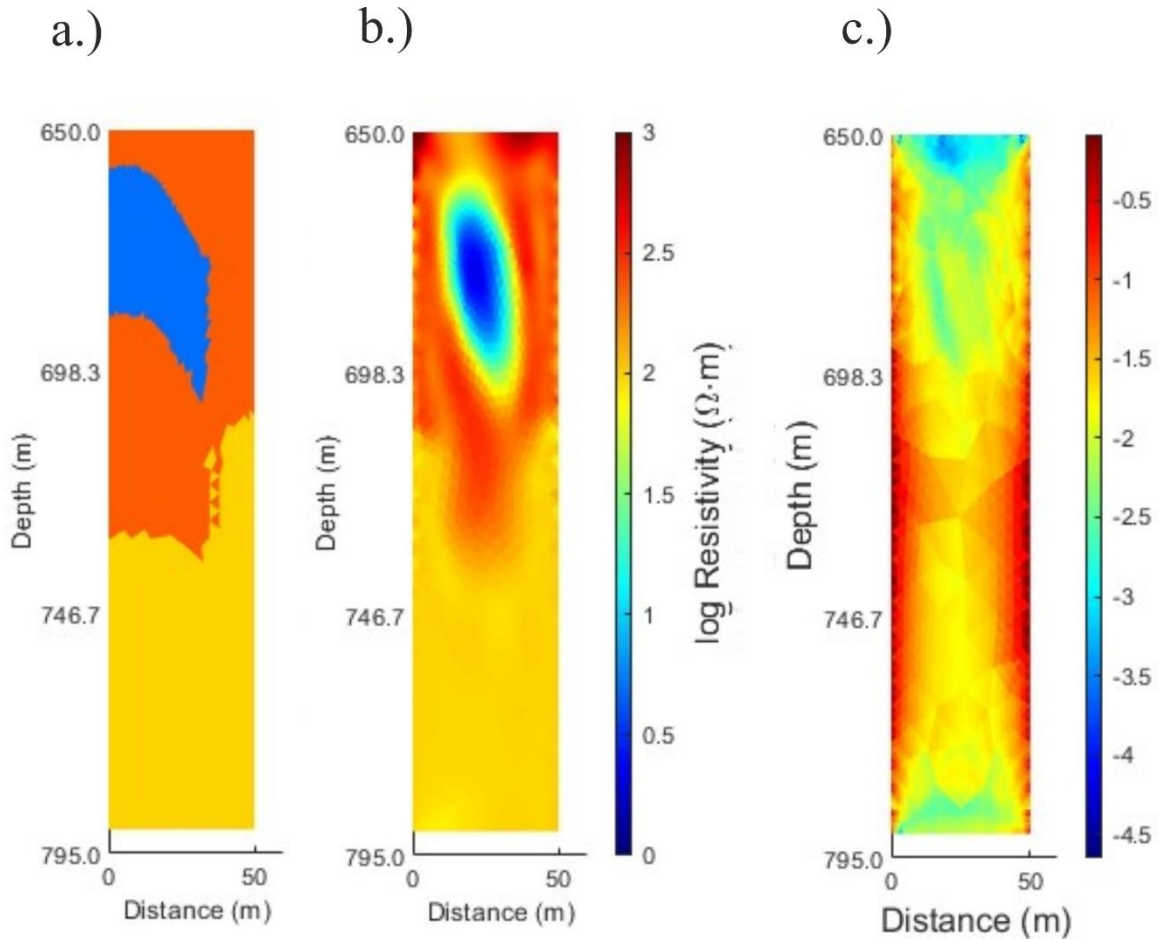


Figure 4. 12 (a) Synthetic model representing a heterogeneous medium characterized by diverse resistivity values. Initially, at time t_1 , the resistivity values of the layers were as follows: approximately 223.87223.87 ohm-m for both the first and second layers, while the third and fourth layers exhibited resistivities of 100 ohm-m each. (b) Inverted electrical resistivity imaging model [Ohm-m] based on the synthetic data. (c) Model Resolution Matrix depicting the resolution quality of the inverted model.

4.2.9 Analysis of Model Resolution

Across the synthetic models analyzed, we observed variations in the resolution quality, as indicated by the Model Resolution Matrices. The diagonal elements of these matrices provide a measure of the resolution achieved for each model configuration, with higher values indicating better resolution. By comparing the resolution matrices across different scenarios, considering the variable background resistivity, we can identify optimal conditions for imaging subsurface anomalies and assess the impact of varying resistivity contrasts on resolution quality.

4.2.9 Implications for Subsurface Imaging

The analysis of model resolution provides valuable insights into the capabilities and limitations of the inversion technique in imaging subsurface structures. By understanding the factors influencing resolution quality, such as resistivity distribution and contrast, researchers and practitioners can optimize data acquisition and processing strategies to enhance imaging performance. Additionally, insights gained from model resolution analysis contribute to the development of advanced inversion methodologies tailored to specific geological settings and exploration objectives.

Chapter 5

Conclusions

The study delves into the intricate process of Cross-well Electrical Resistivity Tomography (ERT) inversion and its significance in reconstructing subsurface electrical resistivity or conductivity distributions. By analysing measurements obtained from electrodes placed in different wells, ERT inversion aims to estimate subsurface parameters, often resulting in a "recovered" or "constructed" model through numerical techniques.

Throughout the study, the challenges of ERT inversion, such as its under-determined nature and potential data errors, are addressed. Inversion algorithms and techniques are discussed, highlighting the iterative nature of the process and the importance of minimizing the misfit between observed and predicted data.

Furthermore, The model resolution analysis conducted for a range of synthetic scenarios offers valuable insights into the resolution quality achieved by the inversion technique. By systematically evaluating resolution matrices across different model configurations, considering the variable background resistivity, we gain a comprehensive understanding of the technique's effectiveness in imaging subsurface anomalies. These findings contribute to the ongoing refinement of inversion methodologies and enhance the reliability of subsurface imaging for various applications, including environmental monitoring, resource exploration, and geological characterization.

The study presents several synthetic models and corresponding inversion results, demonstrating the application of ERT inversion in different subsurface scenarios. These models showcase the ability of ERT inversion to provide insights into the spatial distribution and dynamic behavior of injected substances, such as CO₂, within subsurface environments. Overall, the comprehensive analysis presented in this study underscores the importance of ERT inversion in geophysical exploration and its potential for enhancing our understanding of subsurface geological structures and processes.

References

- Adhikari, P. Y. (2016). Near-surface high resolution imaging of a metallogenic zone in the northern fringe of Dalma volcanics in eastern India using electrical resistivity tomography. *Exploration Geophysics*, 394-400.
- Alumbaugh, D. a. (2000). Image appraisal for 2-D and 3-D electromagnetic inversion. *Geophysics*, 1455-1467.
- Bing, Z. a. (2001). Finite element three dimensional direct current resistivity modelling: accuracy and efficiency considerations. *Geophysical Journal International*, 679-688.
- Binley, A. a. (2005). DC resistivity and induced polarization methods. *Hydrogeophysics*, 129-156.
- Candansayar, M. (2008). Two-dimensional individual and joint inversion of three-and four-electrode array dc resistivity data. *Journal of Geophysics and Engineering*, 290-300.
- Carrigan, M. M. (2013). From conspicuous to considered fashion: A harm-chain approach to the responsibilities of luxury-fashion businesses. *Journal of Marketing Management*, 1277-1307.
- Chen, H. (2022). Exploring subsurface hydrology with electrical resistivity tomography. *Nature Reviews Earth & Environment*, 813-813.
- Daily, W. a. (1991). Cross-borehole resistivity tomography. *Geophysics*, 1228-1235.
- Eklblom, H. (1987). The L1-estimate as limiting case of an Lp-or Huber-estimate. *Statistical data analysis based on the L1-norm and related methods*, 109-116.
- Falcon-Suarez, I. M.-M. (2017). Experimental assessment of pore fluid distribution and geomechanical changes in saline sandstone reservoirs during and after CO2 injection. *International Journal of Greenhouse Gas Control*, 356-369.
- Ishizu, K. G. (2019). Internal structure of a seafloor massive sulfide deposit by electrical resistivity tomography, Okinawa Trough. *Geophysical Research Letters*, 46(20), 11025-11034.
- Li, T. G. (2022). Monitoring CO2 injection at the CaMI Field Research Station using microseismic noise sources. *Journal of Geophysical Research: Solid Earth*.
- Menke, W. (1989). *Geophysical data analysis: Discrete inverse theory (revised)*. San Diego: Academic Press.
- N. Wiwattanachang, P. G. (2011). Monitoring crack development in fiber concrete beam by using electrical. *Journal of Applied Geophysics*, 294-304.
- Oldenburg, D. L. (1998). Applications of geophysical inversions in mineral exploration. *The Leading Edge*, 461-465.

- Prakash, A. a. (2022). Implication of electrical resistivity tomography for precise demarcation of pothole subsidence potential zone over shallow depth coal mine workings. *Journal of the Geological Society of India*, 600-606.
- Raab, T. W.-H. (2020). Development of an Electrical Resistivity Tomography Monitoring Concept for the Svelvik CO₂ Field Lab, Norway. *Advances in Geosciences*, 41-53.
- Schmidt-Hattenberger, C. B. (2013). Electrical resistivity tomography (ERT) for monitoring of CO₂ migration-from tool development to reservoir surveillance at the Ketzin pilot site. *Energy Procedia*, 4268-4275.
- Subsurface Insights*. (n.d.). Retrieved from <https://subsurfaceinsights.com/electrical-resistivity-method/>
- Wagner, F. a. (2018). Fully coupled inversion on a multi-physical reservoir model–Part II: The Ketzin CO₂ storage reservoir. *International Journal of Greenhouse Gas Control*, 273-281.
- Wilson, B. S. (2022). Appraisal of Resistivity Inversion Models With Convolutional Variational Encoder–Decoder Network. *IEEE Transactions on Geoscience and Remote Sensing*, 60,, 1-10.